Article

Developmental Cell

RAB-35 and ARF-6 GTPases Mediate Engulfment and Clearance Following Linker Cell-Type Death

Graphical Abstract

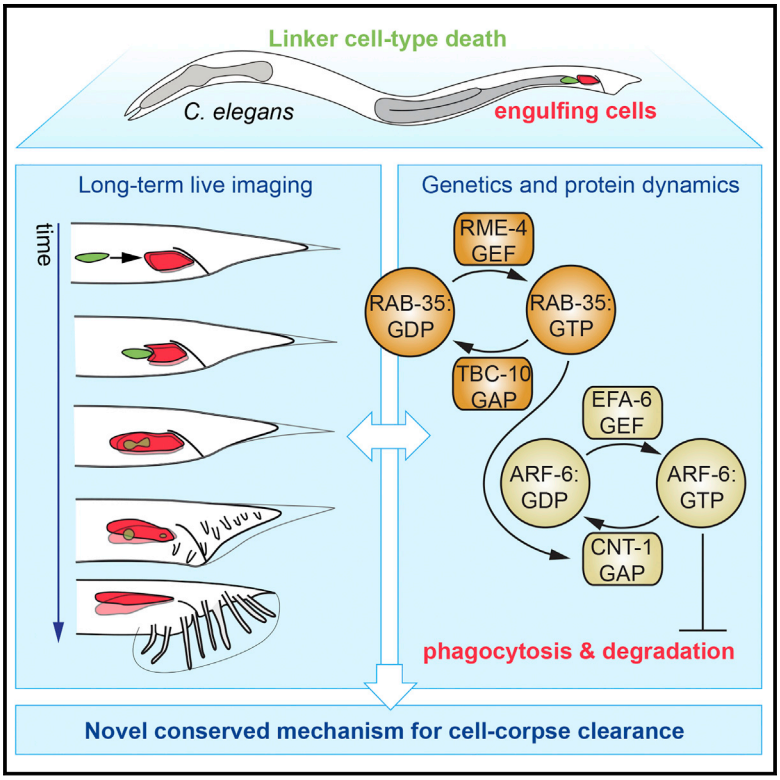

Highlights

- Two cells compete to engulf the *C. elegans* linker cell after linker cell-type death
- Competitive phagocytosis and corpse clearance rely on two small GTPase networks
- RAB-35 removes ARF-6 from phagosome membranes via its regulator CNT-1
- ARF-6 removal promotes $PI(4,5)P_2$ removal and subsequent phagosome maturation

Authors

Lena M. Kutscher, Wolfgang Keil, Shai Shaham

Correspondence

shaham@rockefeller.edu

In Brief

Kutscher et al. discover a protein network for the engulfment and degradation of a *C. elegans* cell that dies by linker cell-type death (LCD). Two cells compete to engulf the cell corpse, relying on two small GTPases, RAB-35 and ARF-6, and their regulators to ensure timely corpse phagocytosis and clearance.

Kutscher et al., 2018, Developmental Cell *47*, 222–238
October 22, 2018
https://doi.org/10.1016/j.devcel.2018.08.015

CellPress

CellPress

Developmental Cell
Article

RAB-35 and ARF-6 GTPases Mediate Engulfment and Clearance Following Linker Cell-Type Death

Lena M. Kutscher,[1] Wolfgang Keil,[1,2] and Shai Shaham[1,3,*]
[1]Laboratory of Developmental Genetics, The Rockefeller University, New York, NY 10065, USA
[2]Center for Studies in Physics and Biology, The Rockefeller University, New York, NY 10065, USA
[3]Lead Contact
*Correspondence: shaham@rockefeller.edu
https://doi.org/10.1016/j.devcel.2018.08.015

SUMMARY

Clearance of dying cells is essential for development and homeostasis. Conserved genes mediate apoptotic cell removal, but whether these genes control non-apoptotic cell removal is a major open question. Linker cell-type death (LCD) is a prevalent non-apoptotic developmental cell death process with features conserved from *C. elegans* to vertebrates. Using microfluidics-based long-term *in vivo* imaging, we show that unlike apoptotic cells, the *C. elegans* linker cell, which dies by LCD, is competitively phagocytosed by two neighboring cells, resulting in cell splitting. Subsequent cell elimination does not require apoptotic engulfment genes. Rather, we find that RAB-35 GTPase is a key coordinator of competitive phagocytosis onset and cell degradation. RAB-35 binds CNT-1, an ARF-6 GTPase activating protein, and removes ARF-6, a degradation inhibitor, from phagosome membranes. This facilitates phosphatidylinositol-4,5-bisphosphate removal from phagosome membranes, promoting phagolysosome maturation. Our studies suggest that RAB-35 and ARF-6 drive a conserved program eliminating cells dying by LCD.

INTRODUCTION

Clearance of cells undergoing programmed cell death is important during development of multicellular organisms, and failure to remove dying cells is implicated in developmental abnormalities (Garlena et al., 2015) and autoimmune disease (Poon et al., 2014). Studies of the nematode Caenorhabditis *elegans* uncovered genes required for engulfment and degradation of cells dying by apoptosis (Ellis et al., 1991; Guo et al., 2010; Kinchen and Ravichandran, 2010; Kinchen et al., 2008; Mangahas et al., 2008; Yu et al., 2008). Homologous genes regulate apoptotic cell clearance in *Drosophila* and vertebrates, as do a number of species-specific genes (Franc et al., 1999; Park and Kim, 2017; Tosello-Trampont et al., 2001).

While caspase-dependent apoptosis is a common cell death mode, recent studies demonstrate that caspase-independent non-apoptotic cell death processes are equally relevant in development (Kutscher and Shaham, 2017) and in disease (Fuchs and Steller, 2015). While the molecular and genetic characterization of some non-apoptotic cell death processes has advanced considerably, whether common clearance mechanisms are used for apoptotic and non-apoptotic dying cells remains a major open question.

LCD (linker cell-type death) is a non-apoptotic developmental cell-death process that is morphologically conserved from *C. elegans* to mammals (Kutscher and Shaham, 2017). This cell death process is characterized by nuclear envelope crenellation, lack of chromatin condensation, and swelling of cytoplasmic organelles. These hallmarks of LCD are prevalent in vertebrate developmental settings, including degeneration of the Wolffian and Müllerian ducts during female and male gonadal development, respectively (Djehiche et al., 1994; Dyche, 1979; Price et al., 1977), and motor neuron elimination during spinal cord formation (Chu-Wang and Oppenheim, 1978). LCD morphology is also characteristic of dying cells in several disease states, including striatal neuron death in Huntington's disease (Maat-Schieman et al., 1999).

During *C. elegans* development, the male-specific linker cell leads the elongation of the developing gonad and eventually dies by LCD (Abraham et al., 2007). Linker cell death is independent of caspases and all known apoptosis, necrosis, and autophagy genes. A network of proteins governing linker cell death has been uncovered, converging on the stress-induced transcription factor HSF-1, acting in a stress-independent manner to promote expression of LET-70/UBE2D2, an E2 ubiquitin ligase. LET-70/UBE2D2, together with other components of the ubiquitin proteasome system, then drive LCD and linker cell clearance (Blum et al., 2012; Kinet et al., 2016; Malin et al., 2016). Following LCD initiation, the linker cell is engulfed (Sulston et al., 1980). The linker cell, therefore, is a particularly attractive *in vivo* model for investigating the clearance of a cell that normally dies non-apoptotically: the time of linker cell death onset is predictable, the process can be followed in live animals, and engulfment events can be dissected genetically.

Here, we show that engulfment and degradation of the linker cell differ in mechanics and genetics from apoptotic cell clearance. We demonstrate that, unlike apoptotic cell corpses, the linker cell is simultaneously engulfed by two U cell-descendent phagocytes, resulting in cell splitting. Apoptotic engulfment genes are not required for this form of engulfment. Rather, we find that the GTPase RAB-35, not previously implicated in apoptotic corpse removal, is a key coordinator of at least two steps in linker cell degradation. Early on, RAB-35 localizes to

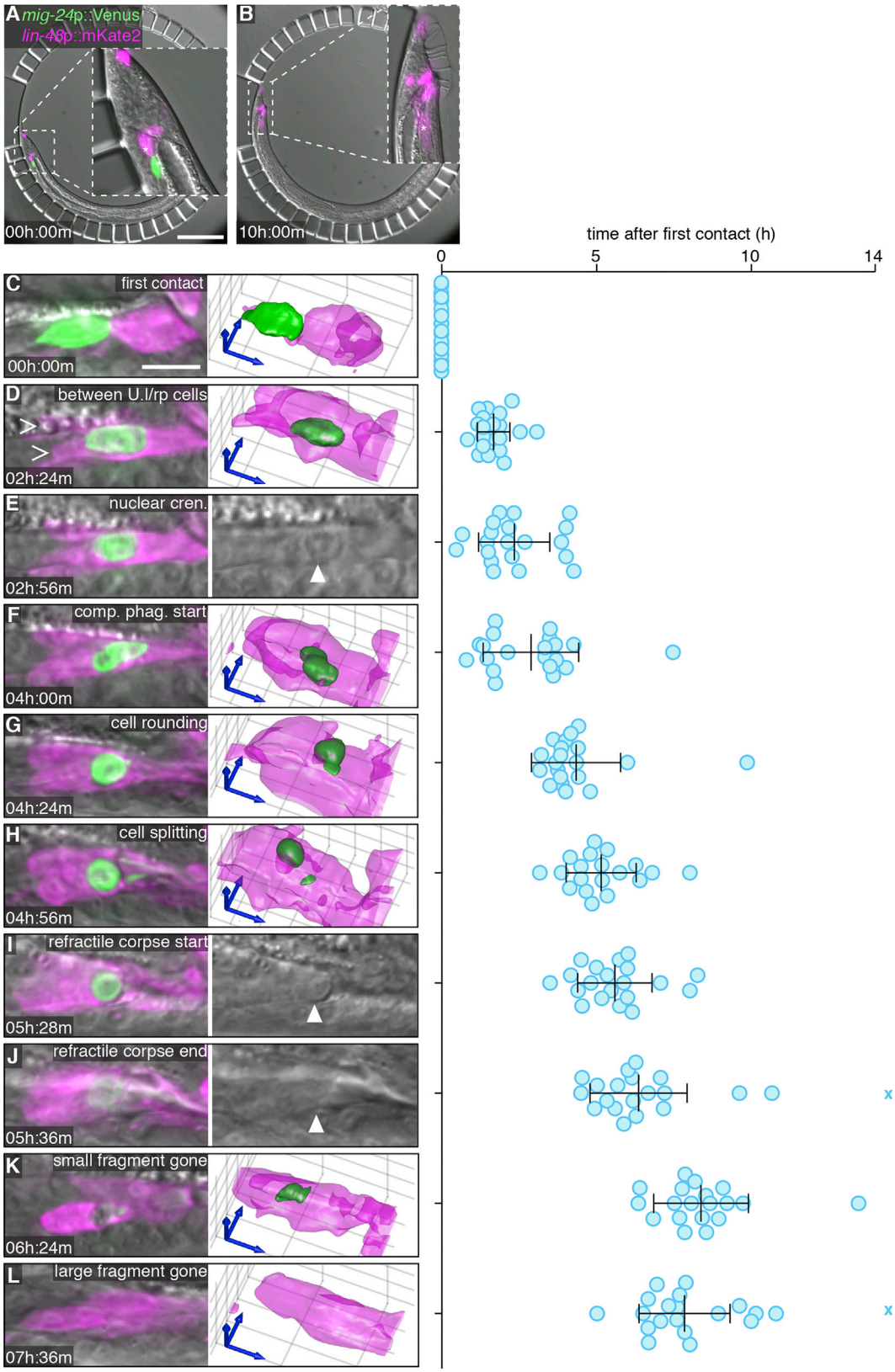

Figure 1. Linker Cell Death and Degradation

(A and B) *C. elegans* male immobilized in a microfluidic chamber (see Keil et al., 2017) at (A) first contact between linker cell (green) and engulfing U.l/rp cell (magenta, asterisk) and (B) after 10 hr. All males examined in all figures carry the male-producing *him-5*(*e1490*) or *him-8*(*e1489*) mutation. Scale bar, 100 μm.

(legend continued on next page)

extending phagocyte pseudopods and prevents premature onset of phagocytosis. Then, RAB-35 drives degradation of the linker cell by promoting the removal of phosphatidylinositol 4,5-bisphosphate ($PI(4,5)P_2$) from the nascent phagosome, thereby facilitating recruitment of RAB-5 and RAB-7 GTPases onto phagosome membranes. We demonstrate that both activities of RAB-35 require inactivation of another conserved small GTPase, ARF-6, which we show functions as a clearance inhibitor. RAB-35 physically interacts with the ARF-6 GTPase-activating protein (GAP) CNT-1, providing a plausible mechanism for ARF-6 inhibition. Furthermore, while RAB-35 localizes to engulfing-cell and phagosome membranes during most of linker cell clearance, ARF-6 only transiently persists at the membrane, and its removal coincides with the removal of $PI(4,5)P_2$ from the phagosome membrane. Both ARF-6 and $PI(4,5)P_2$ removal depend on RAB-35.

RAB-35 and ARF-6 have been previously suggested to promote engulfment of bacteria by cultured cells (Egami et al., 2011); however, neither protein has been studied for roles in the removal of dying cells. Furthermore, the *in vivo* mechanisms by which these proteins promote engulfment have not been dissected. Our work establishes a powerful *in vivo* model to study phagocytosis of cells that die non-apoptotically in development and suggests that different phagocytic pathways can target cells that die by different means.

RESULTS

The Dying Linker Cell Is Simultaneously Engulfed by Two Neighboring Cells

Linker cell death and clearance occurs during the transition from the fourth larval stage to the adult and can take up to 8 hr to complete (Abraham et al., 2007; Keil et al., 2017). To examine this process at high spatiotemporal resolution, we used a long-term imaging microfluidic device we previously developed (Keil et al., 2017) to simultaneously image the linker cell (*mig-24*p::Venus) and the engulfing cells (*lin-48*p::mKate2) in live animals (Figures 1A and 1B). Animals were loaded into the device, and z-stacks were acquired every 8 min for >20 hr (Figure 1A). Animal development and linker cell death kinetics were not affected by either imaging or fluorescent reporter identity (Figure 1B; Table S1, top; see also Keil et al., 2017). There was no significant photobleaching of the U.l/rp engulfing cells or other cells labeled by the *lin-48*p reporter over the duration of imaging (Figures 1A and 1B), but the intensity of YFP in the dying linker cell decreased as the cell was engulfed, degraded, and eventually removed, as expected (Figures 1C–1K). The timings of characteristic events accompanying linker cell degradation were noted, with time zero corresponding to the time of first contact between the linker cell and the U.lp or U.rp engulfing cells (Figure 1C; Video S1), and are consistent with previous reports (Abraham et al., 2007; Keil et al., 2017).

We found that after first contact, the linker cell migrates so that it becomes sandwiched between the U.lp and U.rp cells (carets, Figure 1D; Video S2A), whose cell nuclei are displaced anterior to the linker cell. Linker cell nuclear crenellation also becomes apparent at this time (Figure 1E). Remarkably, following linker cell nuclear changes, both U.l/rp cells simultaneously attempt to engulf the linker cell (Figures 1F and S1A–S1D; Video S2B). During this process, which we term "competitive phagocytosis," linker cell rounding (Figure 1G) is followed by splitting of the linker cell into two fragments (Figures 1H, S1E, and S1F; Video S2C). The larger linker cell remnant contains the nucleus and is equally likely to be found within U.lp or U.rp (8/19 and 11/19, respectively; $p = 0.5$, χ^2 test). The cell engulfing the nucleus-containing fragment is more likely to be binucleate (17/19; $p = 0.0006$, χ^2 test), a result of an earlier unrelated U cell descendent fusion event (Sulston et al., 1980), suggesting that the larger U.l/rp cell engulfs a larger portion of the linker cell. The larger linker cell remnant, but not the smaller, then becomes refractile by DIC microscopy (Figures 1I and 1J). The two linker cell fragments are degraded with similar kinetics (Figures 1K and 1L). Competitive phagocytosis does not result in extensive leakage of linker cell cytoplasm, as we never observed reporter protein outside the cell ($n = 35$).

To identify the precise time point at which the linker cell fragments become internalized, we followed linker cell death in animals expressing the mKate2-PH reporter, derived from PLC-δ1, which marks the plasma membrane and membranes of open phagosomes by binding phosphatidylinositol (4,5)-bisphosphate ($PI(4,5)P_2$) (Botelho et al., 2000; Cheng et al., 2015). Localization of this reporter around the linker cell ceases 14 ± 12.6 min prior to cell splitting ($n = 8$, Figures S1G–S1J), suggesting that cell splitting coincides with the onset of phagosome maturation.

The unique mechanics governing linker cell dismantling raise the question of whether U cell descendants are specifically equipped for linker cell clearance. To test this, we examined animals carrying a mutation in the gene *him-4*, in which linker cell migration is defective and the cell ends up near the head (Abraham et al., 2007). In these animals, linker cell death occurs fairly reliably, as determined by the onset of nuclear crenellation (Abraham et al., 2007). However, while engulfment and degradation by neighboring cells can occur, it is inefficient (62% ± 6.9% corpses remaining in 24-hr adult males, $n = 50$, $p < 0.0001$ compared to wild-type, Fisher's exact test). Thus, U.l/rp cells exhibit specialization for linker cell clearance.

Apoptotic Engulfment Genes Are Not Required for Linker Cell Clearance

It was previously reported that linker cell engulfment can occur in animals lacking apoptosis engulfment genes (Abraham et al., 2007); however, whether the cell is eventually degraded in these settings was not examined. To look at this in detail, we followed linker cell engulfment in animals lacking components of each or

(C) Left: maximum intensity projection showing linker cell at first contact with U.l/rp cells. Right: 3D rendering. Scale bar, 10 μm.
(D–L) Stereotypical events during linker cell dismantling. Images as in (C), except that in (E), (I), and (J), a single DIC slice is shown instead of 3D rendering. Right, time of events in individual animals (blue circles) after first contact. X, event did not occur during imaging. Bars, mean ± SD. Arrowhead, linker cell. (D) Linker cell between U.l/rp cells (caret). (E) Nuclear crenellation onset. (F) Competitive phagocytosis begins. (G) Linker cell rounding. (H) Linker cell corpse splits. (I) The onset of refractility. (J) End of refractility. (K) Small fragment disappears. (L) Large fragment disappears.
See also Videos S1 and S2; Figure S1; and Table S1.

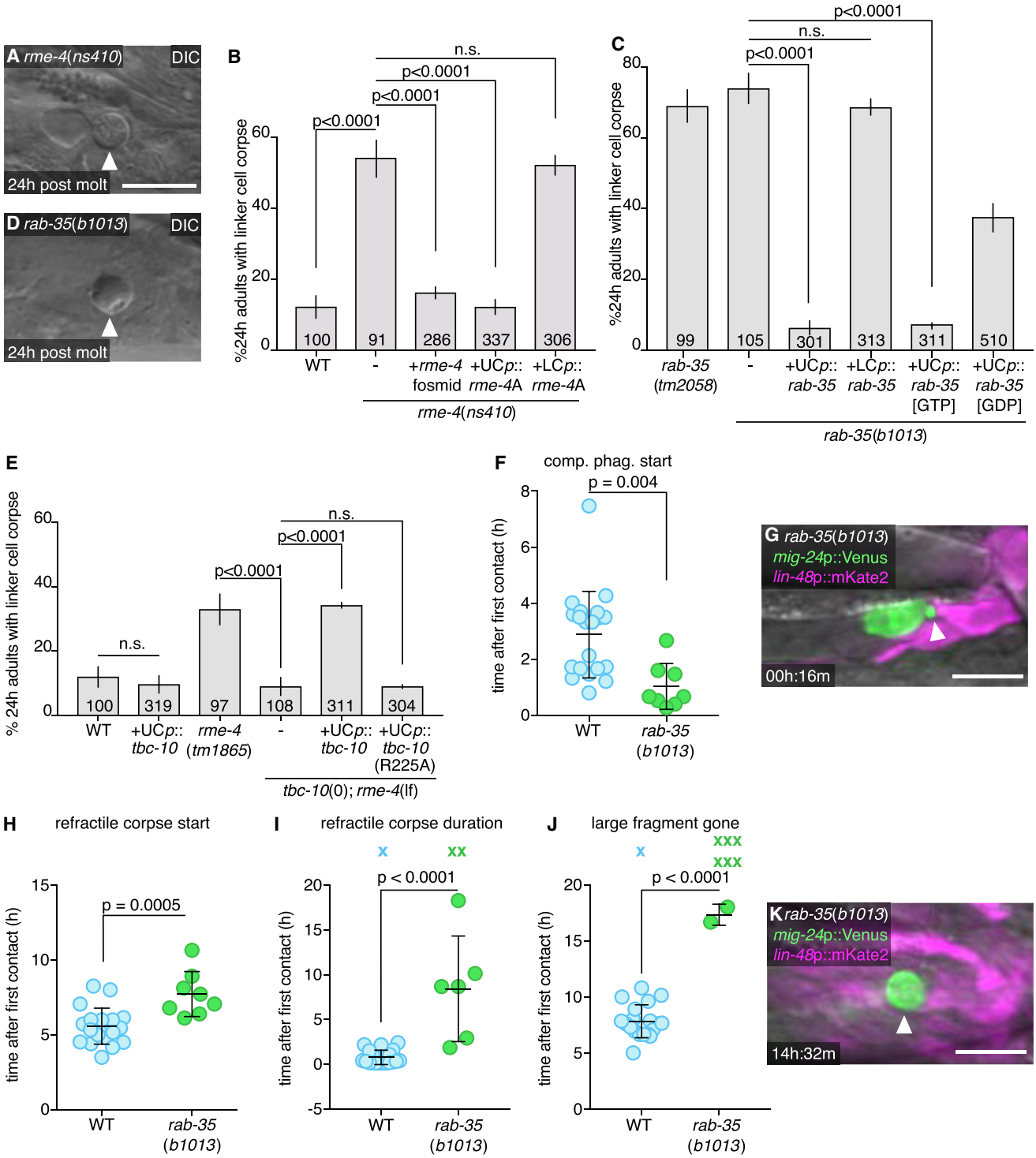

Figure 2. RAB-35, RME-4 (DENND1), and TBC-10 (TBC10D1A) Regulate Linker Cell Clearance

(A) DIC image of persistent linker cell corpse (arrowhead) in *rme-4*(*ns410*). Scale bar, 10 μm.

(B and C) Linker cell degradation in indicated genotypes. Strains contain *lag-2*p::GFP linker cell reporter and *him-5*(*e1490*). UCp, *lin-48*p. LCp, *mig-24*p. The number of animals scored inside bars. Average of at least three independent lines. Error bars, standard error of the proportion or standard error of the mean. n.s., $p > 0.05$, Fisher's exact test.

(D) DIC image of persistent linker cell corpse (arrowhead) in *rab-35*(*b1013*).

(E) Histogram details as in (B).

(F) Competitive phagocytosis onset in individual animals (circles). Bars, mean ± SD. Student's t test. WT, wild-type.

(legend continued on next page)

both parallel pathways that together drive apoptotic cell engulfment. Animals were scored 24 hr after the L4-to-adult transition, when the majority of animals have cleared the linker cell corpse (Keil et al., 2017). We found that linker cell removal is only weakly perturbed by mutations in some known engulfment genes (Table S2). Furthermore, double mutants between engulfment genes in different pathways do not strongly affect linker cell clearance. Consistent with this observation, when we expressed MFG-E8-GFP, a phosphatidylserine-binding protein (Andersen et al., 2000; Venegas and Zhou, 2007), in U cell descendants, we did not observe fluorescence accumulation around the linker cell (5 lines, >100 animals scored in total). Nonetheless, we did find that mutations in the phagosome maturation gene *sand-1*, which is involved in the RAB-5 to RAB-7 conversion in phagosome maturation (Kinchen and Ravichandran, 2010), and in *rab-7*, a RAB protein responsible for the recruitment of late endosomes and lysosomes to the phagosome (Kinchen et al., 2008), significantly inhibited clearance of linker cell debris (Table S2).

Thus, while some genes promoting cell corpse degradation following engulfment are shared between LCD and apoptosis, upstream genes required for phagocytosis and the initiation of degradation are different. LCD-specific engulfment and degradation genes remain, therefore, to be discovered.

RME-4/DENND1 Promotes Linker Cell Engulfment and Degradation

To identify components of the linker cell corpse removal machinery, we sought mutants in which linker cell engulfment and/or degradation is defective. To do so, we mutagenized hermaphrodites carrying a *lag-2*p::GFP linker cell reporter and a *him-5* mutation, which increases the proportion of male progeny (Figure S1K). After two generations, males were screened for linker cell persistence. We previously showed that animals defective in linker cell death exhibit gonadal blockage and can be sterile (Abraham et al., 2007). We therefore directly collected sperm from mutant males by impaling a needle into the gonad and used this sperm to artificially inseminate wild-type hermaphrodites (LaMunyon and Ward, 1994) (Figures S1L–S1N; see STAR Methods for details). Cross progeny were then used to establish mutant lines.

From this screen, we identified a mutant, *ns410*, which exhibits persistent refractile linker cell corpses (Figures 2A and 2B). Using standard genetic mapping, coupled with whole genome sequencing, we identified a mutation predicted to generate a G100E alteration in the DENN domain protein RME-4, homologous to vertebrate DENND1 (Sato et al., 2008) (Figure S2A). Linker cell degradation is restored in *ns410* mutants by expressing a fosmid spanning the genomic region of *rme-4* (Figure 2B). Furthermore, two other *rme-4* alleles, *ns412* (S217N; isolated in our screen) and *b1001* (G257D; a previously characterized loss-of-function lesion [Sato et al., 2008]), also cause linker cell degradation defects, as does the *rme-4(tm1865)* deletion allele (Figure S2B). *rme-4*(*tm1865*) mutants exhibit a weaker linker cell survival defect, perhaps because the truncated RME-4 protein produced in this mutant is present at half wild-type levels (Sato et al., 2008). RNAi against *rme-4* exacerbates the defect of animals carrying this allele (Figure S2B). Taken together, these results demonstrate that the *rme-4* gene is required for linker cell corpse degradation.

RME-4 is widely expressed and found in the linker cell and in its engulfing cells (Figure S2C). To determine where RME-4 functions, we expressed cDNAs for either the *rme-4*A or *rme-4*B transcript (Figure S2A) in either the linker cell or the engulfing cells. We found that the longer A isoform restores linker cell degradation when expressed in U cell descendants, but not when expressed in the linker cell (Figure 2B). B isoform expression in the engulfing cells has no effect (Figure S2B). Thus, RME-4A is the active isoform driving linker cell engulfment, and it does so by acting in the engulfing cells.

RAB-35 GTPase Is a Key Linker Cell Degradation Regulator Controlled by RME-4/DENND1 and TBC-10/TBC1D10A

The RME-4 DENN domain was previously proposed to drive the guanine nucleotide exchange reaction of the small GTPase RAB-35 (Allaire et al., 2010; Sato et al., 2008). The *ns410*, *ns412*, and *b1001 rme-4* alleles are predicted to cause single amino-acid changes within this domain, suggesting that RME-4 could function as a GEF during linker cell degradation. To test this directly, we examined two *rab-35* mutants, *tm2058* and *b1013*, that carry a small deletion surrounding the start codon and an early Q69Ochre stop mutation, respectively (Figure S2D). We found that both lesions inhibit linker cell corpse degradation and that persistent corpses resemble those seen in *rme-4* mutants (Figures 2C and 2D). While *rab-35* is broadly expressed (Figure S2E), we found that linker cell degradation is restored to *rab-35* mutants by expression of *rab-35* cDNA in engulfing cells but not in the linker cell (Figure 2C). Thus, RAB-35 is required in engulfing cells for linker cell degradation.

Rab35 functions were previously studied in *in vitro* models of macrophage phagocytosis of IgG-opsonized erythrocytes and of zymosan (Egami et al., 2011, 2015). Activation-inactivation cycles of RAB-35 were found to be important (Egami et al., 2015), but neither the GEF nor the GAP driving these cycles was identified. Furthermore, downstream consequences of Rab35 loss were not explored. We, therefore, sought to determine which regulatory proteins control RAB-35 activity and how RAB-35 functions in phagosome maturation.

If RME-4 functions as a RAB-35 GEF, we expect RAB-35[GTP] to be the active form of the protein in linker cell degradation. Indeed, we found that expression of RAB-35(Q69L), predicted to lock the

(G) Arrowhead, early competitive phagocytosis in *rab-35*(*b1013*). Details as in Figure 1. Scale bar, 10 μm.
(H) Onset of refractile corpse in individual animals (circles). Bars, mean ± SD. Student's t test. WT, wild-type.
(I) Refractile corpse duration in individual animals (circles). Bars, mean ± SD. Student's t test. WT, wild-type. X, Event persisting or not observed by end of imaging; not included in statistical analysis.
(J) Removal of large fragment in individual animals (circles). Bars, mean ± SD. Student's t test. WT, wild-type. X, Event persisting or not observed by end of imaging; not included in statistical analysis.
(K) Arrowhead, persistent large cell fragment in *rab-35*(*b1013*). Strain and image details as in (G). Scale bar, 10 μm.
See also Video S3; Figures S2 and S3; and Tables S1 and S4.

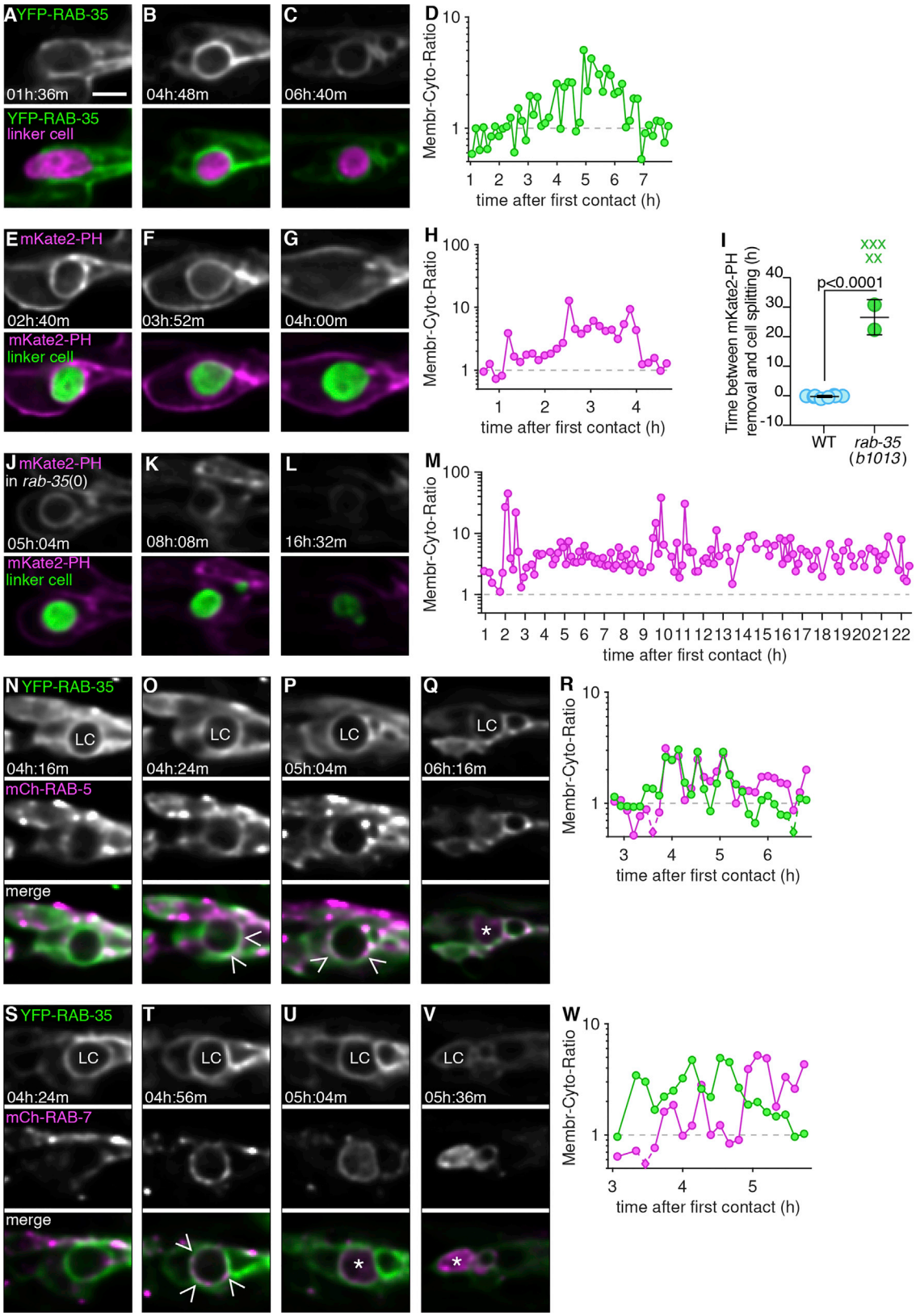

(legend on next page)

protein in the GTP-bound configuration, fully restores linker cell degradation to *rab-35*(*b1013*) mutants (Figure 2C). A GDP-bound mimetic, RAB-35(S24N), however, only partially rescues *rab-35*(*b1013*) linker cell defects. Furthermore, we found that the RAB-35(S24N) protein selectively binds RME-4A (but not RME-4B) in a yeast two-hybrid assay (Sato et al., 2008) (Figure S2F). Thus, RAB-35 functions with RME-4 in engulfing cells, and RAB-35[GTP] is likely the relevant active form driving linker cell clearance.

We next sought to identify the GAP completing the RAB-35 GTPase cycle. We reasoned as follows: weak RME-4 (GEF) mutations should result in some RAB-35[GTP] production, but perhaps not enough for efficient linker cell degradation. Combining an *rme-4*(weak) mutation with a RAB-35 GAP mutation, which would block RAB-35[GTP] hydrolysis, could, however, allow sufficient accumulation of RAB-35[GTP] for efficient linker cell degradation. We therefore screened for the effects of mutations in *C. elegans* homologs of the known mammalian Rab35 GAP genes identified in the context of endocytosis, *tbc-7/Tbc1D24, tbc-10/Tbc1D10A*, and *tbc-13/Tbc1D13* (Chaineau et al., 2013). Mutations or knockdown of these genes alone have no effect on linker cell corpse degradation, nor do they rescue linker cell degradation defects of animals carrying the strong *rme-4*(*ns410*) mutation, in which no RAB-35[GTP] is predicted to accumulate (Figure S2G). However, combining the *tbc-10*(*gk388086*) allele with the weak *rme-4*(*tm1865*) allele restores normal linker cell degradation (Figure 2E). Thus, TBC-10 is likely the RAB-35 GAP for linker cell engulfment and degradation.

Supporting this notion, while TBC-10 protein is widely expressed (Figure S2H), specific expression of TBC-10 in U cell descendants of *rme-4*(*tm1865*); *tbc-10*(*gk388086*) double mutants reintroduces the linker cell degradation defect. Similar expression of a TBC-10(R225A) protein, containing a lesion in the putative catalytic arginine finger, has no effect (Figure 2E).

Taken together, our results suggest that RAB-35[GTP] is a key regulator of linker cell degradation and that its activity is controlled by RME-4/GEF and TBC-10/GAP.

RAB-35 Promotes Timely Onset of Linker Cell Engulfment and Is Required for Subsequent Phagosome Maturation

To define more specifically the defects associated with loss of RAB-35, we imaged *rab-35*(*b1013*) mutants using the microfluidic setup and quantified hallmark linker cell death and degradation events over >24 hr (Video S3 and Table S1). We found no significant differences compared to wild-type animals in the onset or duration of developmental milestones (e.g., tail-tip retraction or the appearance of rays; Figures S3A–S3C) or in the appearance of linker cell death hallmarks (e.g., nuclear crenellation; Figures S3D–S3I). However, competitive phagocytosis of the linker cell begins prematurely in *rab-35* mutants (Figure 2F), initiating before the linker cell has the opportunity to intercalate between the U.l/rp cells (Figure 2G). While subsequent linker cell splitting occurs at the same time as in wild-type animals (Figure S3G), formation of the larger refractile corpse is delayed (Figure 2H), and refractility can last much longer (Figure 2I). Mutations in *rab-35* delay degradation of the large fragment if it occurs at all (Figures 2J and 2K). The smaller linker cell fragment is degraded as in the wild-type (Figures S3H and S3I). Thus, RAB-35 plays roles in both engulfment initiation and phagosome maturation, but not phagosome closure.

Consistent with a role in engulfment initiation, we found that RAB-35, tagged with the fluorescent reporter YFP, localizes to extending pseudopods early on and remains enriched around the larger linker cell-containing phagosome for an extended period of time until late stages of linker cell degradation (Figures 3A–3C). To track this quantitatively, we measured YFP fluorescence on the phagosomal membrane and in the cytoplasm of the U.l/rp cell containing the large fragment and calculated their ratios over time (Figure 3D).

Some aspects of phagosome maturation have been previously characterized. We therefore sought to address where in this process RAB-35 functions. The conversion of $PI(4,5)P_2$ to PI(3)P at the phagosome membrane is necessary for phagosome maturation to proceed (Lu and Zhou, 2012). We therefore imaged an mKate2-PH reporter, marking $PI(4,5)P_2$. While in wild-type animals, $PI(4,5)P_2$ removal occurs just prior to cell splitting (Figures 3E–3H), in the absence of *rab-35*, $PI(4,5)P_2$ removal occurs much later if it occurs at all (23.7 ± 7.1 hr; Figures 3I–3M, note time stamps on image frames).

Because linker cell degradation in *rab*-35 mutants is blocked at a very early stage of phagosome maturation, we sought to determine whether defects in the recruitment of other maturation factors are also evident. To do so, we first characterized wild-type animals expressing both YFP-RAB-35 and either mCherry-RAB-5, marking early phagosomes, or mCherry-RAB-7, marking

Figure 3. RAB-35 Is Required for $PI(4,5)P_2$ Removal and Is Enriched with RAB-5

(A–C) Top: localization of YFP-RAB-35 within U.l/rp cells. Bottom: YFP-RAB-35 (green), and linker cell (*mig-24*p::mKate2; magenta). Scale bar, 5 μm.

(D) The ratio of average fluorescence intensity on phagosome membrane over the cytoplasm in hr after the first contact of the animal shown in adjacent images. The logarithmic scale, where 1 indicates an equal amount of cytoplasmic and phagosome membrane-bound fluorescence. Any data point with a ratio below 0.5 is indicated with a diamond and dotted line.

(E–G) The same format as (A), except mKate2-PH is imaged and the linker cell is fluorescently labeled with YFP.

(H) Same format as (D).

(I) The timing of mKate2-PH removal in relation to linker cell splitting in individual animals (circles). Bars, mean ± SD. Student's t test. WT, wild-type. X, cell splitting occurred, but mKate2-PH was not removed and not included in statistical analysis.

(J–L) Same format as (E) except in *rab-35*(*b1013*) animal.

(M) Same format as in (D).

(N–Q) Same format as (A), except mCherry-RAB-5 is imaged and the linker cell is not fluorescently labeled. Caret, site of colocalization. LC, linker cell. Asterisk, accumulation within phagosome.

(R) Same format as in (D).

(S–V) Same format as (A), except mCherry-RAB-7 is imaged and the linker cell is not fluorescently labeled. Caret, site of colocalization; LC, linker cell; asterisk, accumulation within phagosome.

(W) Same format as in (D).

See also Figure S4 and Table S1.

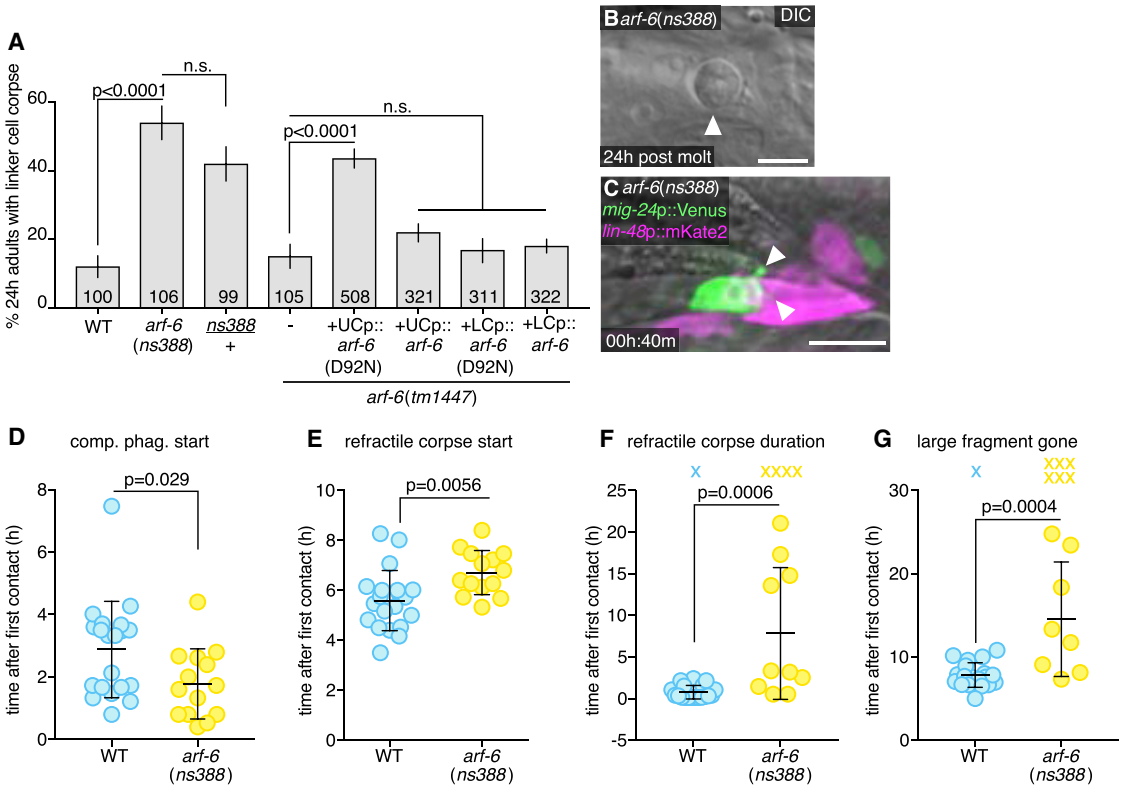

Figure 4. ARF-6 Inhibits Linker Cell Degradation

(A) Linker cell degradation in indicated genotypes. Details as in Figure 2B.

(B) DIC image of persistent linker cell corpse (arrowhead) in *arf-6*(*ns388*) male. Scale bar, 5 μm.

(C) Arrowheads, premature competitive phagocytosis in *arf-6*(*ns388*). Scale bar, 10 μm.

(D–G) The timing of linker cell clearance events in *arf-6*(ns388). Quantification as in Figures 2F and 2H–2J.

See also Video S4; Figures S3 and S5; and Table S1.

late phagosomes and phagolysosomes (Figures 3N–3W; Table S1). We found that RAB-35 and RAB-5 were co-enriched on phagosome membranes in 5/6 animals examined (Figures 3O, 3P, and 3R). mCherry-RAB-5 accumulates within the phagosome after co-enrichment (Figure 3Q; 6/6 animals). While RAB-35 and RAB-7 are also initially enriched on the membrane at a similar time, RAB-7 enrichment increases after RAB-35 is removed (Figures 3T and 3W; 7/7 animals). Once RAB-35 disappears from the phagosome membrane, mCherry-RAB-7 fluorescence accumulates within the phagosome (Figures 3U and 3V; 7/7 animals). Internalization initiates while the linker cell corpse is still round (Figure 3U) and is still evident as the linker cell phagosome changes shape and is degraded (Figure 3V; shape changes observed also by DIC microscopy). Such internalization of RAB-5 and RAB-7 had not been previously reported in other settings, and we believe it cannot be attributed to general differences in fluorescence levels during imaging, as our ratiometric quantification (e.g., Figures 3R and 3W) is independent of overall fluorescence levels. Furthermore, RAB-35, RAB-5, and RAB-7 reporter fusion fluorescence is stable in other cells labeled in our strains.

We next examined reporter localization in *rab-35*(*b1013*) mutants. We found that when the linker cell is not properly cleared, RAB-5 rarely accumulates on the phagosome surface, its enrichment there is not sustained, and it is not internalized into the phagosome (Figures S4A–S4D; 6/8 animals). RAB-7 does not accumulate on the phagosome surface at all and is also not taken up into the phagosome (Figures S4E–S4H; 5/5 animals). These results suggest that RAB-35 is required for RAB-5 and RAB-7 recruitment to the phagosome membrane, consistent with an early block in phagosome maturation. Supporting this notion, *rab-35*(*b1013*); *sand-1*(*ok1963*) double mutants almost completely abrogate linker cell degradation, further implicating RAB-35 in phagosome maturation (*sand-1*(*ok1963*); *rab-35* (*b1013*): 95% ± 2.7% remaining corpses, n = 63, $p < 0.0001$ compared to single mutants, Fisher's exact test).

Our studies, therefore, support the idea that RAB-35 acts early in phagosome maturation to remove $PI(4,5)P_2$ and recruit RAB-5 and RAB-7 to the phagosome membrane for proper degradation to ensue.

The Small GTPase ARF-6 Blocks Linker Cell Clearance

To delineate the molecular mechanism by which RAB-35 controls linker cell engulfment onset and degradation, we pursued studies of another mutant, *ns388*, isolated in our genetic screen. Animals carrying this lesion have similar linker cell defects to *rab-35* mutants (Figures 4A and 4B) but do not harbor mutations in *rab-35*, *tbc-10*, or *rme-4*.

Using whole genome sequencing and standard genetic mapping, we found that *ns388* animals contain a point mutation predicted to cause a D92N mutation in the small GTPase ARF-6 (Figure S5A). Importantly, and unlike *rab-35* mutations, a single *arf-6*(*ns388*) allele is sufficient to block linker cell degradation. Thus, *arf-6*(*ns388*) is a dominant allele (Figure 4A). The *arf-6*(*tm1447*) putative null allele, which lacks most of the coding region and has no ARF-6 expression by western blot (Shi et al., 2012), exhibits normal linker cell clearance (Figure 4A), suggesting that *arf-6*(*ns388*) is a gain-of-function and not a dominant-negative allele. To confirm that *arf-6* is indeed the relevant gene, we generated two independent CRISPR alleles, *ns751* and *ns752*, recreating the *arf-6*(*ns388*) lesion. Both promote linker cell defects similar to those of *arf-6*(*ns388*) mutants (Figure S5B). Furthermore, while *arf-6* is widely expressed (Figures S5C and S5D), expression of an *arf-6*(*ns388*) cDNA in engulfing cells blocks linker cell clearance (Figure 4A). Wild-type *arf-6* expression in engulfing cells does not affect linker cell death, nor does expression of either *arf-6*(*ns388*) or *arf-6*(+) cDNAs in the linker cell (Figure 4A).

Our results therefore demonstrate that gain of ARF-6 function blocks linker cell clearance and suggest that ARF-6 normally functions as a linker cell clearance inhibitor.

ARF-6(gf) Promotes Premature Competitive Phagocytosis Onset and Delays Linker Cell Degradation

ARF-6 has also been previously implicated in macrophage phagocytosis of foreign particles, but the exact mechanism by which it does this was unexplored (Egami et al., 2011, 2015). To understand how ARF-6(gf) interferes with linker cell clearance, we imaged *arf-6*(*ns388*) animals in our microfluidic device and followed hallmark linker cell death and degradation events (Video S4; Table S1). Except for a slight advance in cuticle shedding, no defects in animal development or linker cell killing are seen in *arf-6*(*ns388*) mutants (Figure S3). However, as with *rab-35* mutants, premature onset of competitive phagocytosis is observed (Figures 4C and 4D), formation of a refractile linker cell corpse is delayed (Figure 4E), and the period of linker cell refractility is prolonged (Figure 4F). Degradation of the large linker cell fragment is greatly delayed, if it occurs at all (Figure 4G).

The similar defects exhibited by *arf-6*(*ns388*) and *rab-35* mutants suggest that the proteins encoded by these genes may localize in a similar manner. To test this idea, we expressed ARF-6-YFP in the U.l/rp cells and followed its localization during linker cell death and degradation (Figures 5A–5D). ARF-6-YFP localizes to U.l/rp pseudopods (Figure 5A; Table S1), remains enriched on the phagosome membrane until immediately prior to cell splitting (removal occurs 18.7 ± 14.9 min prior to cell splitting, Figure 4B), and then rapidly translocates to intracellular puncta (Figure 5C). Removal of ARF-6-YFP occurs at a similar time as $PI(4,5)P_2$ removal and coincides with enrichment of mCherry-RAB-5 around the phagosome (Figures 5J–5N; 5/6 animals). RAB-5 also accumulates in the phagosome interior (Figure 5M; 6/6 animals). Similar to *rab-35* mutants, in *arf-6*(gf) mutants, removal of $PI(4,5)P_2$ occurs slowly, if at all (11.5 ± 4.4 hr, Figures 5E–5L; note time stamps on images); and RAB-5 recruitment does not occur (Figures 5O–5R; 4/5 animals), suggesting an early block in phagosome maturation. Thus, both ARF-6 and RAB-35 localize to the plasma membrane early and surround the dying linker cell. However, while RAB-35 normally promotes linker cell degradation, ARF-6 blocks this process.

ARF-6 Function Is Regulated by CNT-1/ACAP2 and EFA-6/EFA6

To understand the dominant nature of the ARF-6(D92N) lesion, we attempted to assess the consequences of locking ARF-6 protein in the GTP- or GDP-bound states (Macia et al., 2004). We first used CRISPR to generate *arf-6* mutants encoding T44N and Q67L mutations (Figure S5A), predicted to accumulate ARF-6[GDP] or ARF-6[GTP] proteins, respectively. However, neither mutant exhibits linker cell defects, and the *arf-6*(Q67L) allele unexpectedly behaves as a null in genetic assays (see below). Nonetheless, we did serendipitously isolate from our CRISPR mutagenesis an *arf-6*(I42M,P43T) double mutant with linker cell clearance defects. Based on an Arf6:Arf6GAP co-crystal protein structure (Ismail et al., 2010), these lesions may interfere with GAP binding to ARF-6 and subsequent GTP hydrolysis. D92 of Arf6 forms intramolecular hydrogen bonds with R95 (Figure 6A). In the D92N mutant, these hydrogen bonds are lost (Figure 6B), which may result in loss of stability of adjacent interactions. Both P43 and I42 of Arf6 form hydrophobic interactions with W451 and I462 on the ArfGAP (Figure 6C). These interactions are lost in the P43T;I42M mutations (Figure 6D). Therefore, ARF-6[GTP] appears to inhibit phagosome maturation during linker cell clearance, and the mutants we isolated may hinder GAP binding.

If this idea is correct, then mutations in a relevant ARF-6 GAP should also exhibit linker cell clearance defects, as they would lock ARF-6 in the GTP-bound state. From a screen of candidate mutations (Figure 6E; Table S3), we found that two independent putative null alleles of *cnt-1*, encoding a ubiquitously expressed protein similar to vertebrate Acap2, block linker cell clearance (Figures 6E, S5E, and S5F). Expression of the CNT-1A isoform in U.l/rp cells, but not in the linker cell, fully rescues linker cell defects of *cnt-1* mutants (Figure 6F), whereas CNT-1B expression gives partial rescue (Figure S5G). Rescue is abolished by mutating the catalytic arginine of CNT-1A (Figure 6F). Importantly, ARF-6 is required for the linker cell defects of *cnt-1* mutants, as an *arf-6*(*tm1447*) loss-of-function mutation restores linker cell clearance to *cnt-1* mutants (Figure 6E). Consistent with the idea that the D92N and I42M;P43T mutations disrupt GAP binding, we found that while wild-type ARF-6 interacts with CNT-1A (but not CNT-1B) in a yeast two-hybrid assay, both ARF-6(D92N) and ARF-6(I42M;P43T) fail to interact with CNT-1A (Figure 6G). Thus, ARF-6[GTP] is likely the active form of the protein blocking linker cell removal, and CNT-1 is the ARF-6 GAP for linker cell clearance.

Similar reasoning used to identify TBC-10 as a RAB-35 GAP allowed us to identify EFA-6, homologous to the mammalian Arf6 GEF Efa6 (Macia et al., 2001), as the putative ARF-6 GEF for linker cell clearance. While the *efa-6*(*ok3533*) deletion allele has no linker cell degradation defect, this allele restores linker cell clearance to mutants carrying null alleles of *cnt-1* (Figure 6H; *cnt-1*(*tm2313*); *efa-6*(*ok3533*): 14% ± 3.4%, $n = 102$, $p < 0.0001$ compared to *cnt-1*(*tm2313*), Fisher's exact test). Furthermore, *efa-6*(*ok3533*) also blocks the dominant defects of *arf-6*(*ns388*) and *arf-6*(*ns763*[I42M;P43T]) mutants, strengthening our assessment that ARF-6 GTP loading is required for the function of these

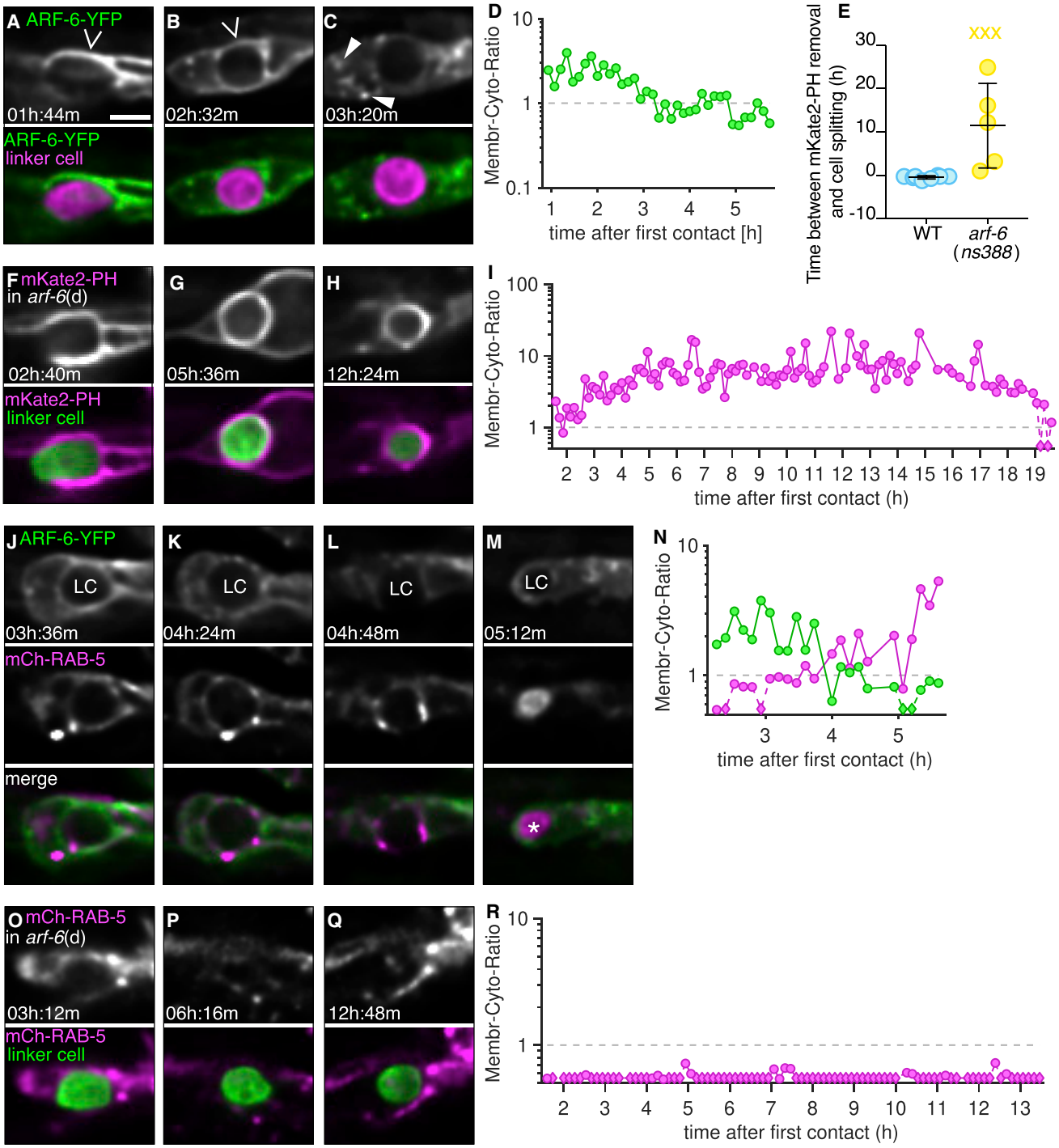

Figure 5. ARF-6(gf) Affects Removal of PI(4,5)P_2 from the Phagosome Membrane and Affects RAB-5 Recruitment

(A–C) Top: localization of ARF-6-YFP within the U.l/rp cells. Caret, ARF-6 on phagosome membrane. Arrowhead, ARF-6 in intracellular puncta. Bottom: ARF-6-YFP (green), and linker cell (*mig-24*p::mKate2; magenta). Scale bar, 5 μm.

(D) The ratio of average fluorescence intensity on phagosome membrane over the cytoplasm in hr after the first contact of animal shown in adjacent images. Logarithmic scale, where 1 indicates an equal amount of cytoplasmic and phagosome membrane-bound fluorescence. Any data point with a ratio below 0.5 is indicated with a diamond and dotted line.

(E) Timing of mKate2-PH removal in relation to linker cell splitting in individual animals (circles). Bars, mean ± SD. Student's t test. WT, wild-type, same data as in Figure 3I. X, cell splitting occurred, but mKate2-PH was not removed and not included in statistical analysis.

(F–H) Same format as (A), except mKate2-PH imaged and the linker cell is fluorescently labeled with YFP.

(I) Same format as (D).

(legend continued on next page)

ARF-6 gain-of-function proteins (Figures 6H and S5H). While EFA-6 is expressed in the linker cell and U.l/rp cells (Figure S5I), expression of EFA-6 isoforms in the U.l/rp cells partially restores linker cell clearance defects to *efa-6*(*ok3533*); *arf-6*(*ns388*) double mutants (Figure S5H). Furthermore, EFA-6 isoforms interact with ARF-6[GDP] in a yeast two-hybrid assay (Figure 6I).

Taken together, our results suggest that ARF-6 inhibits linker cell phagocytosis onset and blocks linker cell degradation together with its regulators EFA-6/GEF and CNT-1A/GAP.

RAB-35 Binds CNT-1A and Drives ARF-6 Removal from Phagosome Membranes

rab-35(0) and *arf-6*(gf) mutants exhibit similar linker cell clearance defects. We wondered, therefore, whether RAB-35 and ARF-6 proteins act in the same pathway, especially since these proteins are implicated together *in vitro* in phagocytosis of foreign particles by macrophages (Egami et al., 2011, 2015). We found that putative null mutations in *arf-6* or *efa-6* almost fully restore linker cell clearance to *rab-35* mutants (Figures 7A and S6A). The *arf-6*[Q67L] CRISPR mutant also suppresses *rab-35*(0) defects (Figure S6B), confirming this allele inactivates ARF-6 and is not an ARF-6[GTP] mimetic (see above). Linker cell clearance defects are restored to *rab-35*(*b1013*); *arf-6*(*tm1447*) double mutants by expressing wild-type *arf-6* in U.l/rp cells, but not in the linker cell (Figure S6C). Furthermore, neither mutations in *cnt-1* nor the dominant *arf-6* allele enhance the linker cell defects of *rab-35* mutants (Figure S6D). Finally, overexpression of YFP-RAB-35 in engulfing cells restores linker cell clearance to *arf-6*(*ns388*) mutants (Figure 7A). Taken together, these results suggest that RAB-35 normally functions to inactivate ARF-6 *in vivo* following linker cell death.

To understand how RAB-35 inhibits ARF-6, we imaged mKate2-RAB-35 and ARF-6-YFP localization together. Consistent with our other imaging studies, the two proteins initially co-localize to extending U.l/rp cell pseudopods (Figure 7C). RAB-35 then accumulates on the phagosome membrane, while ARF-6 enrichment fades (Figures 7D–7G; 8/9 animals). Next, we examined ARF-6-YFP dynamics in *rab-35*(*b1013*) animals. Remarkably, we found that ARF-6-YFP remains on the membrane longer than in wild-type animals (5/6 animals; Figures 7B and 7H–7L; note time stamps; ARF-6-YFP removed 5.4 ± 2.0 hr after cell splitting in *rab-35*(*b1013*)). Furthermore, in wild-type animals, ARF-6(D92N) remains enriched on phagosome membranes longer than ARF-6-YFP (4/4 animals; Figures 7B and 7M–7Q; 15.9 ± 12.2 hr after cell splitting).

These results raise the possibility that RAB-35 promotes linker cell clearance, at least in part, by facilitating ARF-6 removal from the phagosome. Consistent with this notion, an ARF-6(D92N) gain-of-function protein is more effective in blocking linker cell clearance than ARF-6(D92N) lacking a myristoyl group addition sequence required for membrane localization (D'Souza-Schorey and Stahl, 1995) (Figures S6C and S6E).

To determine whether ARF-6 localization is regulated by direct binding to RAB-35, we assessed their interactions in a yeast two-hybrid system (see STAR Methods). While we did not detect any interactions between these two proteins, we found that RAB-35 [GTP], the active form of RAB-35, binds CNT-1A (and not CNT-1B) (Shi et al., 2012) (Figure 7R). Thus, RAB-35 may recruit CNT-1A to phagosome membranes, catalyzing the conversion of active ARF-6[GTP] to inactive ARF-6[GDP], consistent with its previously suggested *in vitro* function (Egami et al., 2011).

The RAB-35/ARF-6 Module Is Not Required for Apoptotic Cell Clearance

Given the roles of RAB-35 and ARF-6 in the clearance of a cell dying by LCD, we wondered whether these proteins play similar roles in apoptotic cell clearance. To test this, we counted the number of persisting apoptotic cells in 3-fold embryos, after nearly all developmental cell death has taken place. In *him-5* mutant control animals, we counted 0.10 ± 0.30 persisting refractile corpses on average (n = 21). In *arf-6*(*ns388*) mutants, 0.47 ± 0.60 corpses were observed (n = 21, p = 0.0131, Student's t-test). *rab-35*(*b1013*) mutants exhibit 0.81 ± 0.92 corpses on average (n = 21, p = 0.0018, Student's t-test). These small defects pale in comparison to defects exhibited by mutants defective in canonical apoptotic engulfment genes (e.g., *ced-7; ced-10* double mutant: 16.8 ± 4.2 corpses, n = 11). Furthermore, *rme-4* mutant embryos we tested have no clearance defects (*ns410*: 0.14 ± 0.36 apoptotic corpses, n = 14; *ns412*: 0.13 ± 0.33 apoptotic corpses, n = 24). We also examined whether *rab-35* mutations exhibit genetic interactions with canonical apoptosis engulfment genes in linker cell death but found no such interactions.

Our results, therefore, demonstrate that the RAB-35/ARF-6 module plays specific roles in dismantling the linker cell that are not shared with the clearance of apoptotic cells in *C. elegans*.

DISCUSSION

An Engulfment and Degradation Pathway for Non-apoptotic Dying Cells

Caspase-dependent apoptosis does not account for many cell death events that occur during animal development. Indeed, mice homozygous for knockout alleles of key apoptotic genes, including caspase-3, caspase-9, Apaf-1, or a triple knockout of Bax, Bak, and Bok, where intrinsic apoptosis is completely abrogated, can survive to adulthood (Honarpour et al., 2000; Ke et al., 2018; Kuida et al., 1998; Lindsten et al., 2000), a surprising observation given the prevalence of cell death in murine development. Inactivation of apoptosis genes also only weakly interferes with degenerative disease progression (Gould et al., 2006). LCD, a non-apoptotic cell death process, is prevalent in vertebrates (Kutscher and Shaham, 2017) and may account for a significant fraction of cell deaths that take place during development and in disease.

(J–M) Localization of ARF-6-YFP (top) and mCherry-RAB-5 (middle). LC, linker cell; asterisk, accumulation of RAB-5 within phagosome.
(N) Same format as (D).
(O–Q) Same format as (J), except in *arf-6*(*ns388*) animal (ARF-6-YFP not imaged).
(R) Same format as (D).
See also Table S1.

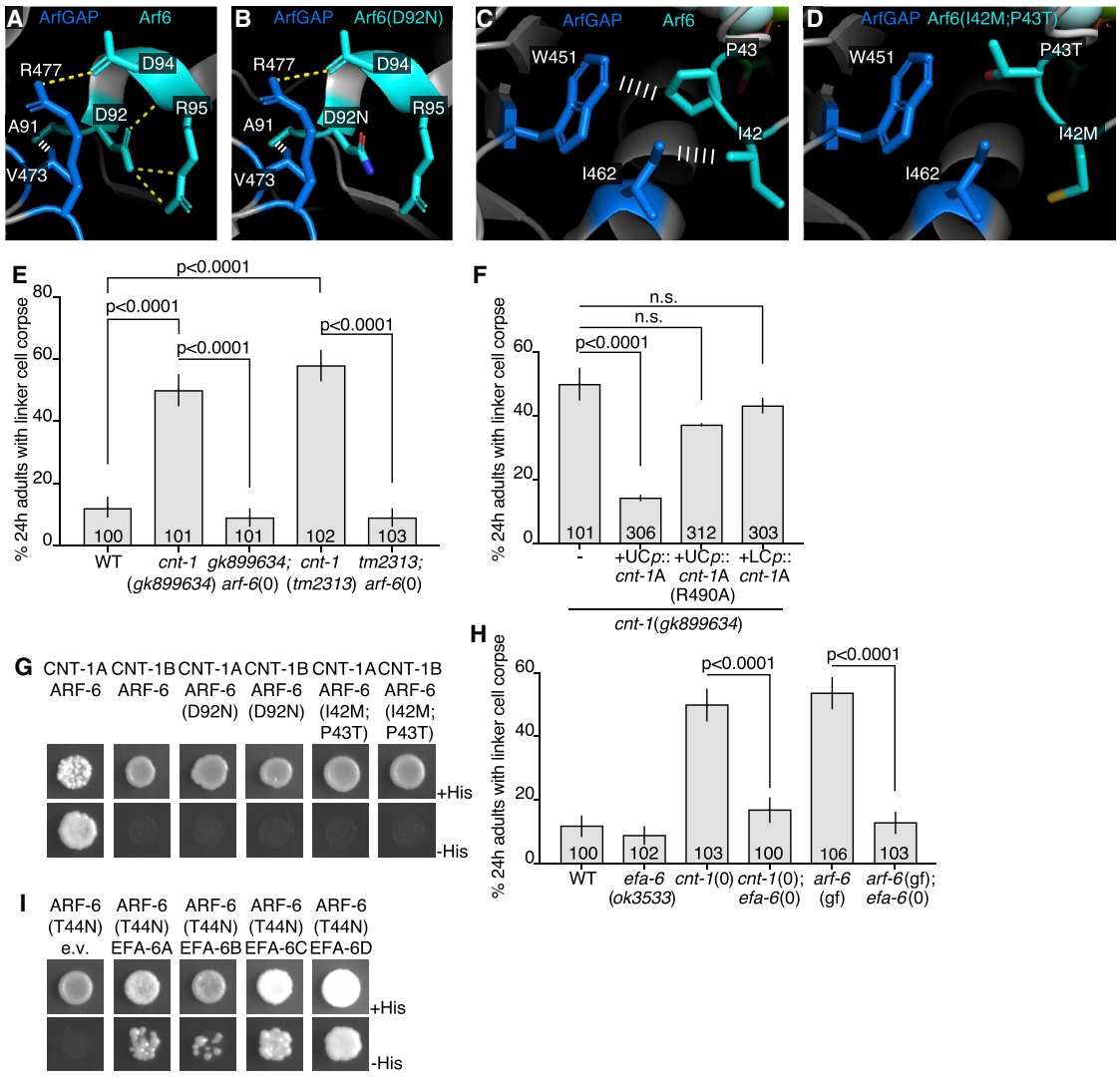

Figure 6. EFA-6 (EFA6) and CNT-1 (ACAP2) Regulate ARF-6

(A) Protein structures of human Arf6 (teal) and ArfGAP (blue) from (Ismail et al., 2010). PDB: 3LVQ. Relevant amino acids are indicated in white. Yellow dotted line, hydrogen bonds. White ladder, hydrophobic interactions. Amino acids shown are conserved in *C. elegans* ARF-6 and CNT-1.

(B) D92N mutation mapped onto Arf6. Protein structure information as in (A).

(C) Different region of Arf6 and ArfGAP. Protein structure information as in (A).

(D) I42M, P43T mutations mapped onto Arf6.

(E and F) Histogram details as in Figure 2B.

(G) Yeast two-hybrid assay with LexA-CNT-1A or LexA-CNT-1B as bait, GAD-ARF-6, GAD-ARF-6(D92N) or GAD-ARF-6(I42M,P43T) as prey. Top: histidine present. Bottom: histidine absent. Growth on -His plates indicates physical interaction.

(H) Histogram details as in (E).

(I) As in (G), with LexA-ARF-6[T44N] (GDP) as bait, GAD-EFA-6A-D as prey.

See also Figure S5 and Table S3.

In this study, we demonstrate that the clearance machinery promoting the removal of the linker cell, which dies by LCD, differs from that used to clear apoptotic cells in *C. elegans*. Our studies uncover a protein network promoting linker cell engulfment and degradation *in vivo* during normal animal development (Figure S6F). We find that RAB-35 and ARF-6 play key early roles, controlling the sequential loading of phagosome maturation factors onto the phagosome membrane, beginning with the removal of PI(4,5)P_2 and continuing with the recruitment of RAB-5 (Figure 7S). Our data are consistent with a model in which RAB-35[GTP] promotes the elimination of dying cells by blocking the activity of an inhibitor of the process, ARF-6[GTP]. Our studies are the first to implicate a RAB-35/ARF-6 module in the engulfment and degradation of dying cells, define in detail multiple accessory factors, identify the relevant targets (e.g., PI(4,5)P_2 removal, RAB-5, RAB-7 recruitment) and, importantly, explore the functions of these proteins *in vivo* in a multicellular organism.

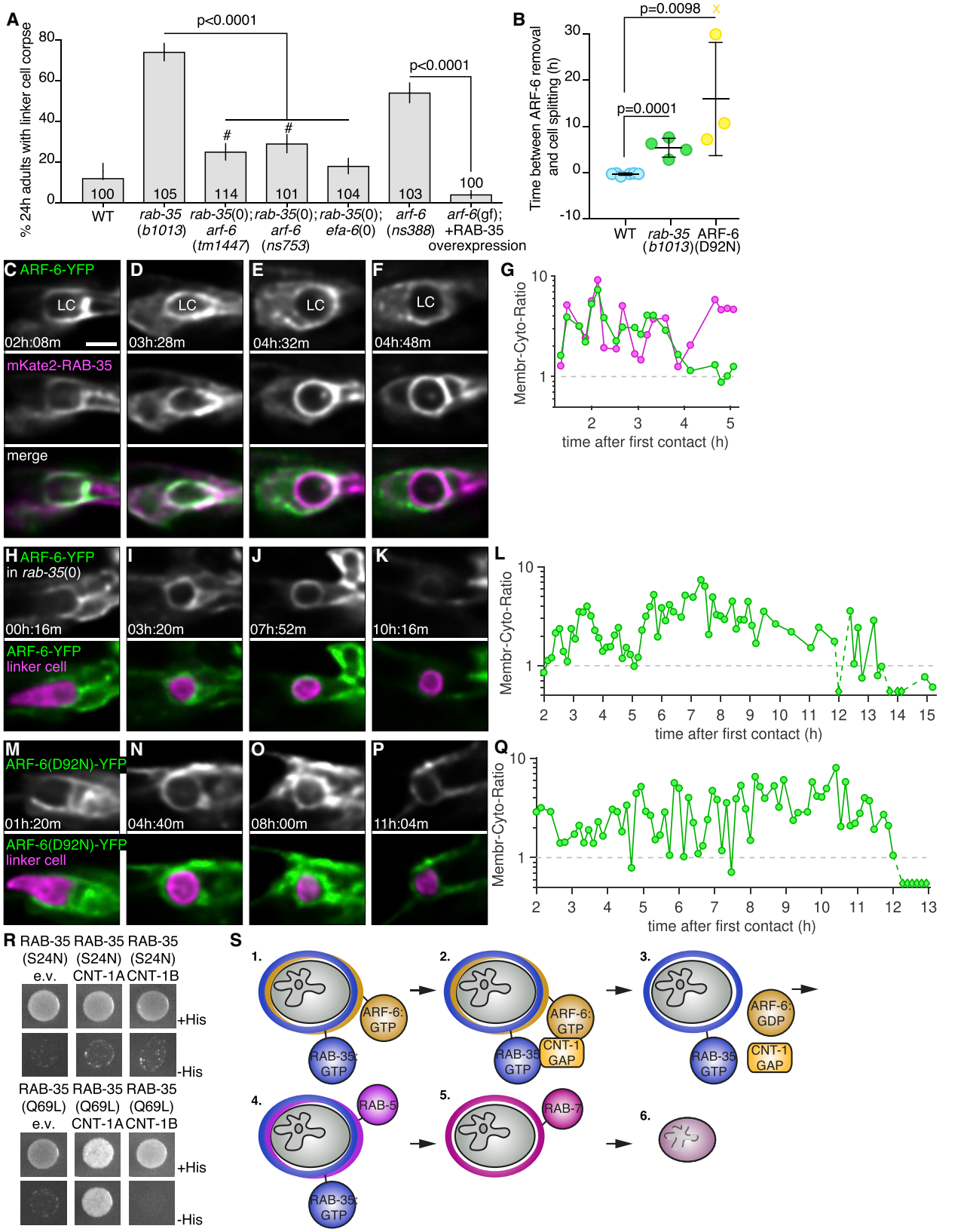

(legend on next page)

Receptor-mediated endocytosis and phagocytosis are two ways by which particles enter a cell. These processes are thought to have generally distinct molecular components, and even shared regulators, such as dynamin, appear to have different functions (De Camilli et al., 1995; Yu et al., 2006). Our findings that RAB-35 and ARF-6 control phagosome PI(4,5)P_2 levels echo a similar role for these proteins in endocytosis (Brown et al., 2001; Cauvin et al., 2016; Honda et al., 1999; Shi et al., 2012), suggesting fundamental similarities between some aspects of these processes.

Although we identify the LCD corpse engulfment pathway in *C. elegans*, a number of studies in other systems raise the possibility that this process may be conserved. For example, in *Drosophila*, nurse cell death is thought to be caspase independent, and knockdown of RAB-35 results in persistent nurse cell nuclei (Timmons et al., 2016). While the molecular function of RAB-35 was not investigated here, the involvement of this protein in a non-apoptotic setting is intriguing, suggesting that the paradigms we found may also function elsewhere in non-apoptotic corpse clearance. Furthermore, concerted activities of RAB-35 and ARF-6 in other contexts have been described, including neurite outgrowth, cytokinesis, oligodendrocyte differentiation, maturation of recycling endosomes, and FcγR-mediated uptake of bacteria by macrophage (Allaire et al., 2013; Chesneau et al., 2012; Egami et al., 2011; Kobayashi and Fukuda, 2012; Miyamoto et al., 2014). In some of these cases, interactions between RAB-35 and putative ARF-6 GAPs are seen (Egami et al., 2015).

Competitive Phagocytosis

In addition to unique molecular components, we found that the mechanics of linker cell engulfment are very different from engulfment of apoptotic cells. Our imaging studies reveal a process of competitive phagocytosis, where two phagocytes compete to engulf portions of the linker cell, resulting in cell splitting. RAB-35 acting through ARF-6 prevents premature activation of this engulfment process. As with the molecular constituents of linker cell engulfment and degradation, we believe that the process of competitive phagocytosis may also be conserved. In macrophage-less mice, for example, mesenchymal cells engulf dying neighbors during digit formation, and occasionally two mesenchymal cells can be seen engulfing the same dying cell in transmission electron microscopy images (Wood et al., 2000). Consistent with this process involving different engulfment regulators, mesenchymal cells do not express the CED-7 homolog ABC1 (Wood et al., 2000). Similarly, in the developing rat cerebellum, more than one non-professional phagocyte can be seen engulfing a dying cell (Parnaik et al., 2000). A related process has been documented during germ cell development in *C. elegans*. Primordial germ cells extend cytoplasm-containing lobes into the adjacent endoderm, and the lobe is excised from the remaining cell, in a process reminiscent of competitive phagocytosis (Abdu et al., 2016).

The need for engulfment by more than one cell could be related to the size of the dying cell. For example, when macrophages attempt to engulf a particle that is too large, engulfment is stalled (Cannon and Swanson, 1992; Herbomel et al., 1999). Engulfment by two or more cells could solve this problem. However, in this case, cytoplasmic spillage must be avoided. The engulfment process we describe here accomplishes exactly that. Intriguingly, the interplay between ARF-6 and RAB-35 in corpse degradation is required only for the larger, nucleus-containing fragment, as the smaller, cytoplasmic-only fragment is degraded efficiently in these mutants. These results suggest that a different mechanism may be required to degrade each of the cellular fragments.

A process reminiscent of competitive phagocytosis can also be seen when cultured human peripheral blood monocytes engulf a *C. albicans* pathogen (Rittig et al., 1998). Similarly, cultured mouse monocytes simultaneously engulf a *Leishmania* parasite (Rittig et al., 1998). One cell engulfs the flagellum, while the other engulfs the posterior pole. In this context, roles for RAB-35 in pathogen clearance (Egami et al., 2011, 2015; Yeo et al., 2016) are especially intriguing and may suggest underlying mechanisms similar to linker cell clearance.

In summary, we demonstrate that engulfment and degradation of a cell that dies by LCD require mechanics and machinery different from that used for apoptotic cell engulfment and degradation and identify a molecular pathway governing this form of cell clearance. Given the conservation of LCD, we propose that this ancillary process may be conserved as well.

STAR★METHODS

Detailed methods are provided in the online version of this paper and include the following:

- KEY RESOURCES TABLE
- CONTACT FOR REAGENT AND RESOURCE SHARING

Figure 7. RAB-35 Removes ARF-6 from Phagolysosome Membranes

(A) Histogram details as in Figure 2B. #, significant difference compared to *rab-35*(*b1013*) and wild-type.

(B) Timing of ARF-6-YFP removal in relation to linker cell splitting in individual animals (circles). Bars, mean ± SD. Student's t test. WT, wild-type. X, cell splitting occurred, but ARF-6-YFP was not removed and not included in statistical analysis. ARF-6(D92N) indicates ARF-6(D92N)-YFP imaged in otherwise WT animals.

(C–F) Localization of indicated proteins with details as in Figure 3. Scale bar, 5 μm.

(G) The ratio of membrane-localized to the cytoplasmic-localized fluorescent protein with details as in Figure 3.

(H–K) Same details as in (C), in *rab-35*(*b1013*) mutant.

(L) Same format as in (G), in *rab-35*(*b1013*) mutant.

(M–P) Same details as in (C) but with ARF-6(D92N)-YFP variant.

(Q) Same format as in (G).

(R) Yeast two-hybrid assay with LexA-RAB-35[S24N] (GDP) or LexA-RAB-35[Q67L] (GTP) as bait, Gal4-AD (GAD)empty vector, GAD-CNT-1A, or GAD-CNT-1B as prey. Details as in Figure 6G.

(S) (1) ARF-6 and RAB-35 surround the nascent phagosome, marked with PI(4,5)P_2. (2) RAB-35 recruits CNT-1. (3) CNT-1 turns off ARF-6, removing it from the phagosome membrane. RAB-35 remains on the membrane. (4) RAB-5 is recruited. (5) RAB-7 recruitment and RAB-35 loss. (6) The linker cell is degraded once the phagosome fuses with lysosomes.

See also Figures S6 and S7 and Table S1.

SUPPLEMENTAL INFORMATION

Supplemental Information includes six figures, four tables, and four videos and can be found with this article online at https://doi.org/10.1016/j.devcel.2018.08.015.

ACKNOWLEDGMENTS

We thank Zheng Zhou for sharing unpublished results; Barth Grant, Zheng Zhou, Paul Randazzo, Jacqueline Cherfils, and Shohei Mitani for reagents; Nima Tishbi for technical help; Jordan Ward for the extensive Cel1 protocol; and Shaham lab members for discussions and critical reading of the manuscript. Some strains were provided by the CGC, which is funded by the NIH Office of Research Infrastructure Programs (P40 OD010440). This work was supported by an NIH NRSA Training Grant GM066699 to L.M.K.; an HFSP postdoctoral fellowship LT000250/2013-C to W.K.; an NSF grant PHY 1502151 awarded to Eric D. Siggia; and NIH grants R01NS081490, R01HD078703, and R35NS105094 to S.S.

AUTHOR CONTRIBUTIONS

Conceptualization, L.M.K. and S.S.; Methodology, L.M.K., W.K., and S.S.; Software, W.K.; Formal Analysis, L.M.K. and W.K.; Investigation, L.M.K. and W.K.; Writing – Original Draft, L.M.K. and S.S.; Writing – Review & Editing, L.M.K., W.K., and S.S.; Funding Acquisition, L.M.K., W.K., and S.S.; Resources, L.M.K., W.K., and S.S.; Visualization, L.M.K., W.K., and S.S.; Supervision, S.S.

DECLARATION OF INTERESTS

The authors declare no competing interests.

Received: December 28, 2017
Revised: July 18, 2018
Accepted: August 17, 2018
Published: September 13, 2018

REFERENCES

Abdu, Y., Maniscalco, C., Heddleston, J.M., Chew, T.L., and Nance, J. (2016). Developmentally programmed germ cell remodelling by endodermal cell cannibalism. Nat. Cell Biol. *18*, 1302–1310.

Abraham, M.C., Lu, Y., and Shaham, S. (2007). A morphologically conserved nonapoptotic program promotes linker cell death in *Caenorhabditis elegans*. Dev. Cell *12*, 73–86.

Allaire, P.D., Marat, A.L., Dall'Armi, C., Di Paolo, G., McPherson, P.S., and Ritter, B. (2010). The Connecdenn DENN domain: a GEF for Rab35 mediating cargo-specific exit from early endosomes. Mol. Cell *37*, 370–382.

Allaire, P.D., Seyed Sadr, M., Chaineau, M., Seyed Sadr, E., Konefal, S., Fotouhi, M., Maret, D., Ritter, B., Del Maestro, R.F., and McPherson, P.S. (2013). Interplay between Rab35 and Arf6 controls cargo recycling to coordinate cell adhesion and migration. J. Cell Sci. *126*, 722–731.

Andersen, M.H., Graversen, H., Fedosov, S.N., Petersen, T.E., and Rasmussen, J.T. (2000). Functional analyses of two cellular binding domains of bovine lactadherin. Biochemistry *39*, 6200–6206.

Arribere, J.A., Bell, R.T., Fu, B.X.H., Artiles, K.L., Hartman, P.S., and Fire, A.Z. (2014). Efficient marker-free recovery of custom genetic modifications with CRISPR/Cas9 in *Caenorhabditis elegans*. Genetics *198*, 837–846.

Blum, E.S., Abraham, M.C., Yoshimura, S., Lu, Y., and Shaham, S. (2012). Control of nonapoptotic developmental cell death in *Caenorhabditis elegans* by a polyglutamine-repeat protein. Science *335*, 970–973.

Botelho, R.J., Teruel, M., Dierckman, R., Anderson, R., Wells, A., York, J.D., Meyer, T., and Grinstein, S. (2000). Localized biphasic changes in phosphatidylinositol-4,5-bisphosphate at sites of phagocytosis. J. Cell Biol. *151*, 1353–1368.

Brown, F.D., Rozelle, A.L., Yin, H.L., Balla, T., and Donaldson, J.G. (2001). Phosphatidylinositol 4,5-bisphosphate and Arf6-regulated membrane traffic. J. Cell Biol. *154*, 1007–1017.

Cannon, G.J., and Swanson, J.A. (1992). The macrophage capacity for phagocytosis. J. Cell Sci. *101*, 907–913.

Cauvin, C., Rosendale, M., Gupta-Rossi, N., Rocancourt, M., Larraufie, P., Salomon, R., Perrais, D., and Echard, A. (2016). Rab35 GTPase triggers switch-like recruitment of the Lowe syndrome lipid phosphatase OCRL on newborn endosomes. Curr. Biol. *26*, 120–128.

Chaineau, M., Ioannou, M.S., and McPherson, P.S. (2013). Rab35: GEFs, GAPs and effectors. Traffic *14*, 1109–1117.

Cheng, S., Wang, K., Zou, W., Miao, R., Huang, Y., Wang, H., and Wang, X. (2015). PtdIns(4,5)P_2 and PtdIns3P coordinate to regulate phagosomal sealing for apoptotic cell clearance. J. Cell Biol. *210*, 485–502.

Chesneau, L., Dambournet, D., Machicoane, M., Kouranti, I., Fukuda, M., Goud, B., and Echard, A. (2012). An ARF6/Rab35 GTPase cascade for endocytic recycling and successful cytokinesis. Curr. Biol. *22*, 147–153.

Chu-Wang, I.W., and Oppenheim, R.W. (1978). Cell death of motoneurons in the chick embryo spinal cord. I. A light and electron microscopic study of naturally occurring and induced cell loss during development. J. Comp. Neurol. *177*, 33–57.

D'Souza-Schorey, C., and Stahl, P.D. (1995). Myristoylation is required for the intracellular localization and endocytic function of ARF6. Exp. Cell Res. *221*, 153–159.

De Camilli, P., Takei, K., and McPherson, P.S. (1995). The function of dynamin in endocytosis. Curr. Opin. Neurobiol. *5*, 559–565.

Dickinson, D.J., Ward, J.D., Reiner, D.J., and Goldstein, B. (2013). Engineering the *Caenorhabditis elegans* genome using Cas9-triggered homologous recombination. Nat. Methods *10*, 1028–1034.

Djehiche, B., Segalen, J., and Chambon, Y. (1994). Ultrastructure of mullerian and wolffian ducts of fetal rabbit *in vivo* and in organ culture. Tissue Cell *26*, 323–332.

Dyche, W.J. (1979). A comparative study of the differentiation and involution of the Mullerian duct and Wolffian duct in the male and female fetal mouse. J. Morphol. *162*, 175–209.

Egami, Y., Fujii, M., Kawai, K., Ishikawa, Y., Fukuda, M., and Araki, N. (2015). Activation-inactivation cycling of Rab35 and ARF6 is required for phagocytosis of zymosan in RAW264 macrophages. J. Immunol. Res. *2015*, 429439.

Egami, Y., Fukuda, M., and Araki, N. (2011). Rab35 regulates phagosome formation through recruitment of ACAP2 in macrophages during FcγR-mediated phagocytosis. J. Cell Sci. *124*, 3557–3567.

Ellis, R.E., Jacobson, D.M., and Horvitz, H.R. (1991). Genes required for the engulfment of cell corpses during programmed cell death in *Caenorhabditis elegans*. Genetics *129*, 79–94.

Franc, N.C., Heitzler, P., Ezekowitz, R.A., and White, K. (1999). Requirement for croquemort in phagocytosis of apoptotic cells in Drosophila. Science *284*, 1991–1994.

Fuchs, Y., and Steller, H. (2015). Live to die another way: modes of programmed cell death and the signals emanating from dying cells. Nat. Rev. Mol. Cell Biol. *16*, 329–344.

Garlena, R.A., Lennox, A.L., Baker, L.R., Parsons, T.E., Weinberg, S.M., and Stronach, B.E. (2015). The receptor tyrosine kinase Pvr promotes tissue closure by coordinating corpse removal and epidermal zippering. Development *142*, 3403–3415.

Gould, T.W., Buss, R.R., Vinsant, S., Prevette, D., Sun, W., Knudson, C.M., Milligan, C.E., and Oppenheim, R.W. (2006). Complete dissociation of motor neuron death from motor dysfunction by Bax deletion in a mouse model of ALS. J. Neurosci. *26*, 8774–8786.

Guo, P., Hu, T., Zhang, J., Jiang, S., and Wang, X. (2010). Sequential action of *Caenorhabditis elegans* Rab GTPases regulates phagolysosome formation during apoptotic cell degradation. Proc. Natl. Acad. Sci. USA *107*, 18016–18021.

Herbomel, P., Thisse, B., and Thisse, C. (1999). Ontogeny and behaviour of early macrophages in the zebrafish embryo. Development *126*, 3735–3745.

Honarpour, N., Du, C., Richardson, J.A., Hammer, R.E., Wang, X., and Herz, J. (2000). Adult Apaf-1-deficient mice exhibit male infertility. Dev. Biol. *218*, 248–258.

Honda, A., Nogami, M., Yokozeki, T., Yamazaki, M., Nakamura, H., Watanabe, H., Kawamoto, K., Nakayama, K., Morris, A.J., Frohman, M.A., et al. (1999). Phosphatidylinositol 4-phosphate 5-kinase alpha is a downstream effector of the small G protein ARF6 in membrane ruffle formation. Cell *99*, 521–532.

Ismail, S.A., Vetter, I.R., Sot, B., and Wittinghofer, A. (2010). The structure of an Arf-ArfGAP complex reveals a Ca2+ regulatory mechanism. Cell *141*, 812–821.

Kamath, R.S., Fraser, A.G., Dong, Y., Poulin, G., Durbin, R., Gotta, M., Kanapin, A., Le Bot, N., Moreno, S., Sohrmann, M., et al. (2003). Systematic functional analysis of the *Caenorhabditis elegans* genome using RNAi. Nature *421*, 231–237.

Ke, F.F.S., Vanyai, H.K., Cowan, A.D., Delbridge, A.R.D., Whitehead, L., Grabow, S., Czabotar, P.E., Voss, A.K., and Strasser, A. (2018). Embryogenesis and adult life in the absence of intrinsic apoptosis effectors BAX, BAK, and BOK. Cell *173*, 1217–1230.

Keil, W., Kutscher, L.M., Shaham, S., and Siggia, E.D. (2017). Long-term high-resolution imaging of developing *C. elegans* larvae with microfluidics. Dev. Cell *40*, 202–214.

Kinchen, J.M., and Ravichandran, K.S. (2010). Identification of two evolutionarily conserved genes regulating processing of engulfed apoptotic cells. Nature *464*, 778–782.

Kinchen, J.M., Doukoumetzidis, K., Almendinger, J., Stergiou, L., Tosello-Trampont, A., Sifri, C.D., Hengartner, M.O., and Ravichandran, K.S. (2008). A pathway for phagosome maturation during engulfment of apoptotic cells. Nat. Cell Biol. *10*, 556–566.

Kinet, M.J., Malin, J.A., Abraham, M.C., Blum, E.S., Silverman, M.R., Lu, Y., and Shaham, S. (2016). HSF-1 activates the ubiquitin proteasome system to promote non-apoptotic developmental cell death in *C. elegans*. Elife *5*, 73.

Kobayashi, H., and Fukuda, M. (2012). Rab35 regulates Arf6 activity through centaurin-β2 (ACAP2) during neurite outgrowth. J. Cell Sci. *125*, 2235–2243.

Kuida, K., Haydar, T.F., Kuan, C.Y., Gu, Y., Taya, C., Karasuyama, H., Su, M.S., Rakic, P., and Flavell, R.A. (1998). Reduced apoptosis and cytochrome c-mediated caspase activation in mice lacking caspase 9. Cell *94*, 325–337.

Kutscher, L.M., and Shaham, S. (2014). Forward and reverse mutagenesis in C. elegans. In WormBook, ed. (The C. elegans Research Community), pp. 1–26.

Kutscher, L.M., and Shaham, S. (2017). Non-apoptotic cell death in animal development. Cell Death Differ. *24*, 1326–1336.

LaMunyon, C.W., and Ward, S. (1994). Assessing the viability of mutant and manipulated sperm by artificial insemination of *Caenorhabditis elegans*. Genetics *138*, 689–692.

Lewis, J.A., and Fleming, J.T. (1995). Basic culture methods. Methods Cell Biol. *48*, 3–29.

Lindsten, T., Ross, A.J., King, A., Zong, W.X., Rathmell, J.C., Shiels, H.A., Ulrich, E., Waymire, K.G., Mahar, P., Frauwirth, K., et al. (2000). The combined functions of proapoptotic Bcl-2 family members Bak and Bax are essential for normal development of multiple tissues. Mol. Cell *6*, 1389–1399.

Liu, H., and Naismith, J.H. (2008). An efficient one-step site-directed deletion, insertion, single and multiple-site plasmid mutagenesis protocol. BMC Biotechnol. *8*, 91.

Lu, N., and Zhou, Z. (2012). Membrane trafficking and phagosome maturation during the clearance of apoptotic cells. Int. Rev. Cell Mol. Biol. *293*, 269–309.

Maat-Schieman, M.L.C., Dorsman, J.C., Smoor, M.A., Siesling, S., Van Duinen, S.G., Verschuuren, J.J.G.M., den Dunnen, J.T., Van Ommen, G.-J.B., and Roos, R.A.C. (1999). Distribution of inclusions in neuronal nuclei and dystrophic neurites in Huntington disease brain. J. Neuropathol. Exp. Neurol. *58*, 129–137.

Macia, E., Chabre, M., and Franco, M. (2001). Specificities for the small G proteins ARF1 and ARF6 of the guanine nucleotide exchange factors ARNO and EFA6. J. Biol. Chem. *276*, 24925–24930.

Macia, E., Luton, F., Partisani, M., Cherfils, J., Chardin, P., and Franco, M. (2004). The GDP-bound form of Arf6 is located at the plasma membrane. J. Cell Sci. *117*, 2389–2398.

Malin, J.A., Kinet, M.J., Abraham, M.C., Blum, E.S., and Shaham, S. (2016). Transcriptional control of non-apoptotic developmental cell death in *C. elegans*. Cell Death Differ. *23*, 1985–1994.

Mangahas, P.M., Yu, X., Miller, K.G., and Zhou, Z. (2008). The small GTPase Rab2 functions in the removal of apoptotic cells in *Caenorhabditis elegans*. J. Cell Biol. *180*, 357–373.

Mello, C., and Fire, A. (1995). DNA transformation. Methods Cell Biol. *48*, 451–482.

Miyamoto, Y., Yamamori, N., Torii, T., Tanoue, A., and Yamauchi, J. (2014). Rab35, acting through ACAP2 switching off Arf6, negatively regulates oligodendrocyte differentiation and myelination. Mol. Biol. Cell *25*, 1532–1542.

Park, S.Y., and Kim, I.S. (2017). Engulfment signals and the phagocytic machinery for apoptotic cell clearance. Exp. Mol. Med. *49*, e331.

Parnaik, R., Raff, M.C., and Scholes, J. (2000). Differences between the clearance of apoptotic cells by professional and non-professional phagocytes. Curr. Biol. *10*, 857–860.

Peng, H., Long, F., Liu, X., Kim, S.K., and Myers, E.W. (2008). Straightening *Caenorhabditis elegans* images. Bioinformatics *24*, 234–242.

Poon, I.K.H., Lucas, C.D., Rossi, A.G., and Ravichandran, K.S. (2014). Apoptotic cell clearance: basic biology and therapeutic potential. Nat. Rev. Immunol. *14*, 166–180.

Price, J.M., Donahoe, P.K., Ito, Y., and Hendren, W.H. (1977). Programmed cell death in the Müllerian duct induced by Müllerian inhibiting substance. Am. J. Anat. *149*, 353–375.

Rittig, M.G., Burmester, G.R., and Krause, A. (1998). Coiling phagocytosis: when the zipper jams, the cup is deformed. Trends Microbiol. *6*, 384–388.

Sato, M., Sato, K., Liou, W., Pant, S., Harada, A., and Grant, B.D. (2008). Regulation of endocytic recycling by *C. elegans* Rab35 and its regulator RME-4, a coated-pit protein. EMBO J. *27*, 1183–1196.

Shaham, S. (2009). Galign: a tool for rapid genome polymorphism discovery. PLoS One *4*, e7188.

Shi, A., Liu, O., Koenig, S., Banerjee, R., Chen, C.C.-H., Eimer, S., and Grant, B.D. (2012). RAB-10-GTPase-mediated regulation of endosomal phosphatidylinositol-4,5-bisphosphate. Proc. Natl. Acad. Sci. USA *109*, E2306–E2315.

Sulston, J.E., Albertson, D.G., and Thomson, J.N. (1980). The *Caenorhabditis elegans* male: postembryonic development of nongonadal structures. Dev. Biol. *78*, 542–576.

Timmons, A.K., Mondragon, A.A., Schenkel, C.E., Yalonetskaya, A., Taylor, J.D., Moynihan, K.E., Etchegaray, J.I., Meehan, T.L., and McCall, K. (2016). Phagocytosis genes nonautonomously promote developmental cell death in the Drosophila ovary. Proc. Natl. Acad. Sci. USA *113*, E1246–E1255.

Tosello-Trampont, A.C., Brugnera, E., and Ravichandran, K.S. (2001). Evidence for a conserved role for CRKII and Rac in engulfment of apoptotic cells. J. Biol. Chem. *276*, 13797–13802.

Venegas, V., and Zhou, Z. (2007). Two alternative mechanisms that regulate the presentation of apoptotic cell engulfment signal in *Caenorhabditis elegans*. Mol. Biol. Cell *18*, 3180–3192.

Ward, J.D. (2015). Rapid and precise engineering of the Caenorhabditis elegans genome with lethal mutation co-conversion and inactivation of NHEJ repair. Genetics *199*, 363–377.

Wicks, S.R., Yeh, R.T., Gish, W.R., Waterston, R.H., and Plasterk, R.H. (2001). Rapid gene mapping in *Caenorhabditis elegans* using a high density polymorphism map. Nat. Genet. *28*, 160–164.

Wood, W., Turmaine, M., Weber, R., Camp, V., Maki, R.A., McKercher, S.R., and Martin, P. (2000). Mesenchymal cells engulf and clear apoptotic footplate cells in macrophageless PU.1 null mouse embryos. Development *127*, 5245–5252.

Yeo, J.C., Wall, A.A., Luo, L., and Stow, J.L. (2016). Sequential recruitment of Rab GTPases during early stages of phagocytosis. Cell. Logist. *6*, e1140615.

Yu, X., Lu, N., and Zhou, Z. (2008). Phagocytic receptor CED-1 initiates a signaling pathway for degrading engulfed apoptotic cells. PLoS Biol. *6*, e61.

Yu, X., Odera, S., Chuang, C.H., Lu, N., and Zhou, Z. (2006). *C. elegans* dynamin mediates the signaling of phagocytic receptor CED-1 for the engulfment and degradation of apoptotic cells. Dev. Cell *10*, 743–757.

Zuryn, S., Le Gras, S., Jamet, K., and Jarriault, S. (2010). A strategy for direct mapping and identification of mutations by whole-genome sequencing. Genetics *186*, 427–430.

STAR★METHODS

KEY RESOURCES TABLE

REAGENT or RESOURCE	SOURCE	IDENTIFIER
Bacterial and Virus Strains		
E. coli OP50	Caenorhabditis Genetics Center (CGC); http://cbs.umn.edu/cgc/home	N/A
E. coli HT115	CGC	N/A
E. coli NA22	CGC	N/A
Experimental Models: Organisms/Strains		
S. cerevisiae: NMY51	Dualsystems Biotech	N/A
C. elegans: N2	CGC	N/A
Additional alleles used and/or generated in present study listed in methods.	N/A	N/A
Oligonucleotides		
ARF-6(D92N) sgRNA: 5' CTAAAAACCTGTCTCTATCAG 3'	This study	N/A
ARF-6(T44N) sgRNA: 5' TCAGTGACCACAATGACGA 3'	This study	N/A
ARF-6(Q67L) sgRNA: 5' CTTCAGGACGTCGGCGGAC 3'	This study	N/A
Single stranded repair oligo ARF-6(D92N): 5' aggaaaaaaaccaatttttccgcatttttcgcct aaaaacCTGTCTCTATtAGCaGCGTCCATCACAAAAATGAGCGCCTGAGTTCCT GTGTAATAATGTC 3'	This study	N/A
Single stranded repair oligo ARF-6(T44N): 5' agCAATTCTGTACAAACTGAAGCTCG GGCAATCAGTGACCACAATTCCGAacGTGGGCTTCAATGTGGAGACTGTCA CGTATAAAAATATCAAATTCAACGT 3'	This study	N/A
Single stranded repair oligo ARF-6(Q67L): Q67L 5' ggcctaaaaacccccaaaaaccccaattt ttcttcagGACGTCGGCGGACttGACAAAATTCGACCCCTCTGGCGACATTATTACACAG GAACTCAGGCGCT 3'	This study	N/A
Recombinant DNA		
pDD162	Dickinson et al. (2013)	Addgene
pLMK46: LexA-CNT-1A, Yeast two-hybrid (Y2H)	This study	N/A
pLMK47: LexA-CNT-1B, Y2H	This study	N/A
pLMK48: GAD-ARF-6, Y2H	This study	N/A
pLMK49: GAD-ARF-6(D92N), Y2H	This study	N/A
pLMK50: GAD-ARF-6(I42M,P43T), Y2H	This study	N/A
pLMK51: LexA-ARF-6(T44N), Y2H	This study	N/A
pLMK52: GAD-EFA-6A, Y2H	This study	N/A
pLMK53: GAD-EFA-6B, Y2H	This study	N/A
pLMK54: GAD-EFA-6C, Y2H	This study	N/A
pLMK55: GAD-EFA-6D, Y2H	This study	N/A
pLMK56: LexA-RAB-35(S24N), [GDP], Y2H	This study	N/A
pLMK57: LexA-RAB-35(Q69L), [GTP], Y2H	This study	N/A
pLMK58: GAD-CNT-1A, Y2H	This study	N/A
pLMK59: GAD-CNT-1B, Y2H	This study	N/A
pLMK60: GAD-RME-4A, Y2H	This study	N/A
pLMK61: GAD-RME-4B, Y2H	This study	N/A
pLMK62: *arf-6*[D92N] CRISPR targeting vector, pDD162 backbone	This study	N/A
pLMK63: *arf-6*[T44N] CRISPR targeting vector, pDD162 backbone	This study	N/A
pLMK64: *arf-6*[Q67L] CRISPR targeting vector, pDD162 backbone	This study	N/A

(*Continued on next page*)

Continued

REAGENT or RESOURCE	SOURCE	IDENTIFIER
nsIs653: UV/TMP integration of *nsEx5304*[pLMK10[*lin-48*p::mKate2-PH] (10 ng/ul)+ *unc-119*(+) (25 ng/ul) + pBluescript (65 ng/ul)]	This study	N/A
nsEx4770,-71,-88,-89,4361,4618,4668: rme-4 fosmid (WRM0615bE09) 10 ng/ul + *lin-48*p::*mCh* (25 ng/ul) + pBluescript (65 ng/ul)	This study	N/A
nsEx4721,-22,-16: pLMK11[*lin-48*p::*rme-4a cDNA-SL2-mCh*](20 ng/ul) + *odr-1*p::RFP(+) (20 ng/ul) + pBluescript (60 ng/ul)	This study	N/A
nsEx4559,-60,4748: pLMK12[*mig-24*p::*rme-4a cDNA*](20 ng/ul) + *odr-1*p::RFP(+) (20 ng/ul) + pEB30[lag-2p::mCh] (25 ng/ul) + pBluescript (35 ng/ul)	This study	N/A
nsEx4669,-64,4742: pLMK13[*lin-48*p::*rme-4b cDNA-SL2-mCh*](20 ng/ul) + *odr-1*p::RFP(+) (20 ng/ul) + pBluescript (60 ng/ul)	This study	N/A
pwIs268: *rme-4* translational reporter, gift from B. Grant	Sato et al. (2008)	N/A
nsEx4658,-66,-91: pLMK14[*lin-48*p::*rab-35 cDNA-SL2-mCh*](20 ng/ul) + *odr-1*p::RFP(+) (20 ng/ul) + pBluescript (60 ng/ul)	This study	N/A
nsEx4654,-89,-90: pLMK15[*mig-24*p::*rab-35 cDNA*](20 ng/ul) + *odr-1*p::RFP(+) (20 ng/ul) + pEB30 (25 ng/ul) + pBluescript (35 ng/ul)	This study	N/A
nsEx4813,-16,-47: pLMK16[*mig-24*p::*rab-35*(Q69L) *cDNA*](20 ng/ul) + *odr-1*p::RFP(+) (20 ng/ul) + pEB30 (25 ng/ul) + pBluescript (35 ng/ul)	This study	N/A
nsEx4799,4821,-31,-29,20: pLMK17[*mig-24*p::*rab-35*(S24N) *cDNA*](20 ng/ul) + *odr-1*p::RFP(+) (20 ng/ul) + pEB30 (25 ng/ul) + pBluescript (35 ng/ul)	This study	N/A
pwIs357: *rab-35* translational reporter, gift from B. Grant	Sato et al. (2008)	N/A
nsEx4741,-49,-86, 4937,-81,-82: pLMK18[*lin-48*p::*tbc-10 cDNA-SL2-mCh*](20 ng/ul) + *odr-1*p::RFP(+) (20 ng/ul) + pBluescript (60 ng/ul)	This study	N/A
nsEx5703,-04,-05: pLMK19[*lin-48*p::*tbc-10*(R225A) *cDNA-SL2-mCh*](20 ng/ul) + *odr-1*p::RFP(+) (20 ng/ul) + pBluescript (60 ng/ul)	This study	N/A
nsIs493: UV/TMP integration of *sEx10170*[rCes R06B10.5::GFP + pCeh361]. Strain BC10170 from CGC.	This study	N/A
nsIs595 V: UV/TMP integration of *nsEx5132*[pLMK20[*lin-48*p::YFP-RAB-35 cDNA] (10 ng/ul)+ *unc-119*(+) (25 ng/ul) + pBluescript (65 ng/ul)]	This study	N/A
nsIs713: UV/TMP integration of [pLMK21[*lin-48*p::mKate2-RAB-35 cDNA] (10 ng/ul)+ *unc-119*(+) (25 ng/ul) + pBluescript (65 ng/ul)]	This study	N/A
nsIs60: *mig-24*p::Venus + *unc-119*(+), a gift from M. Abraham	This study	N/A
nsIs622 X: UV/TMP integration of *nsEx4724*[pLMK22[*lin-48*p::mCherry-RAB-5 cDNA] (1 ng/ul)+ *unc-119*(+) (25 ng/ul) + pBluescript (74 ng/ul)]	This study	N/A
nsIs592 V: UV/TMP integration of *nsEx5610*[pLMK23[*lin-48*p::mCherry-RAB-7 cDNA] (1 ng/ul)+ *unc-119*(+) (25 ng/ul) + pBluescript (74 ng/ul)]	This study	N/A
nsIs586 V: UV/TMP integration of *nsEx5798*[pLMK24[*lin-48*p::CTNS-1-mKate2 cDNA] (10 ng/ul)+ *unc-119*(+) (25 ng/ul) + pBluescript (65 ng/ul)]	This study	N/A
nsEx4717,-38,4848, 4564,-82,-83: pLMK25[*lin-48*p::*arf-6 cDNA-SL2-mCh*](20 ng/ul) + *odr-1*p::RFP(+) (20 ng/ul) + pBluescript (60 ng/ul)	This study	N/A
nsEx4657,-60,4753,-85,-50: pLMK26[*lin-48*p::*arf-6(D92N) cDNA-SL2-mCh*](20 ng/ul) + *odr-1*p::RFP(+) (20 ng/ul) + pBluescript (60 ng/ul)	This study	N/A
nsEx4825,-44,-45, 4815,-46,-49: pLMK27[*mig-24*p::*arf-6 cDNA*](20 ng/ul) + *odr-1*p::RFP(+) (20 ng/ul) + pEB30 (25 ng/ul) + pBluescript (35 ng/ul)	This study	N/A
nsEx4787,-94, 4814: pLMK28[*mig-24*p::*arf-6(D92N) cDNA*](20 ng/ul) + *odr-1*p::RFP(+) (20 ng/ul) + pEB30 (25 ng/ul) + pBluescript (35 ng/ul)	This study	N/A
nsEx4595: pLMK29[*arf-6*p::*arf-6* genomic DNA-GFP-*unc-54* 3'UTR] (10 ng/ul) + *unc-119*(+) (25 ng/ul) + pBluescript (65 ng/ul)	This study	N/A
nsEx4602: pLMK30[*arf-6*p::*arf-6*(ns388) genomic DNA-GFP-*unc-54* 3'UTR] (10 ng/ul) + *unc-119*(+) (25 ng/ul) + pBluescript (65 ng/ul)	This study	N/A
nsEx4953,-48, 5612, 5106,-10,-14,-59: pLMK31[*lin-48*p::*arf-6(ΔG2) cDNA-SL2-mCh*](20 ng/ul) + *odr-1*p::RFP(+) (20 ng/ul) + pBluescript (60 ng/ul)	This study	N/A
nsEx4954,-67,5696: pLMK32[*lin-48*p::*arf-6(ΔG2, D92N) cDNA-SL2-mCh*](20 ng/ul) + *odr-1*p::RFP(+) (20 ng/ul) + pBluescript (60 ng/ul)	This study	N/A

(*Continued on next page*)

Continued

REAGENT or RESOURCE	SOURCE	IDENTIFIER
nsEx5694,-95: pLMK33[*lin-48*p::*cnt-1a cDNA-SL2-mCh*](20 ng/ul) + *odr-1*p::RFP(+) (20 ng/ul) + pBluescript (60 ng/ul)	This study	N/A
nsEx4951,-52,-5692: pLMK34[*mig-24*p::*cnt-1a cDNA*](20 ng/ul) + *odr-1*p::RFP(+) (20 ng/ul) + pEB30 (25 ng/ul) + pBluescript (35 ng/ul)	This study	N/A
nsEx5740,-42,-58: pLMK35[*lin-48*p::*cnt-1a(R490A) cDNA-SL2-mCh*](20 ng/ul) + *odr-1*p::RFP(+) (20 ng/ul) + pBluescript (60 ng/ul)	This study	N/A
nsEx5741,-44,-60: pLMK36[*lin-48*p::*cnt-1b cDNA-SL2-mCh*](20 ng/ul) + *odr-1*p::RFP(+) (20 ng/ul) + pBluescript (60 ng/ul)	This study	N/A
nsEx4938,-49,-50: pLMK37[*mig-24*p::*cnt-1b cDNA*](20 ng/ul) + *odr-1*p::RFP(+) (20 ng/ul) + pEB30 (25 ng/ul) + pBluescript (35 ng/ul)	This study	N/A
nsEx5757: pLMK38[*cnt-1*p::GFP] (10 ng/ul) + *unc-119*(+) (25 ng/ul) + pBluescript (65 ng/ul)	This study	N/A
nsEx5743,-56,-59: pLMK39[*lin-48*p::*efa-6a cDNA-SL2-mCh*](20 ng/ul) + *odr-1*p::RFP(+) (20 ng/ul) + pBluescript (60 ng/ul)	This study	N/A
nsEx5133,-51,-52: pLMK40[*lin-48*p::*efa-6b cDNA-SL2-mCh*](20 ng/ul) + *odr-1*p::RFP(+) (20 ng/ul) + pBluescript (60 ng/ul)	This study	N/A
nsEx5139,-47,-5140: pLMK41[*lin-48*p::*efa-6c cDNA-SL2-mCh*](20 ng/ul) + *odr-1*p::RFP(+) (20 ng/ul) + pBluescript (60 ng/ul)	This study	N/A
nsEx5134,-35,-40: pLMK42[*lin-48*p::*efa-6d cDNA-SL2-mCh*](20 ng/ul) + *odr-1*p::RFP(+) (20 ng/ul) + pBluescript (60 ng/ul)	This study	N/A
nsEx5100: pLMK43[*efa-6p*::GFP] (25 ng/ul) + *unc-119*(+) (25 ng/ul) + pBluescript (50 ng/ul)	This study	N/A
nsIs625: UV/TMP integration of *nsEx5136*[pLMK44[*lin-48*p::ARF-6-YFP cDNA] (10 ng/ul)+ *unc-119*(+) (25 ng/ul) + pBluescript (65 ng/ul)]	This study	N/A
nsIs636: UV/TMP integration of *nsEx5130*[pLMK45[*lin-48*p::ARF-6(D92N)-YFP cDNA] (10 ng/ul)+ *unc-119*(+) (25 ng/ul) + pBluescript (65 ng/ul)]	This study	N/A
nsEx4620,-31,-45,-48,-49: pLMK64[*lin-48*p::MFGe8-GFP] (10 ng/ul) + *unc-119*(+) (25 ng/ul) + pBluescript (65 ng/ul)	This study	N/A
Software and Algorithms		
The PyMOL Molecular Graphics System, Version 1.2r3pre	Schrödinger, LLC	N/A
Huygens Essential 3.7.1	Scientific Volume Imaging (SVI)	N/A
MATLAB R2016b	Mathworks	N/A
Prism 7	GraphPad	N/A

CONTACT FOR REAGENT AND RESOURCE SHARING

Further information and requests for resources and reagents should be directed to and will be fulfilled by the Lead Contact, Shai Shaham (shaham@rockefeller.edu).

EXPERIMENTAL MODEL AND SUBJECT DETAILS

C. elegans

C. elegans strains were raised at 20°C on nematode growth medium (NGM) seeded with OP50 bacteria, unless otherwise indicated. Wild-type animals were of the Bristol N2 strain. All strains have one of two mutations that generate a high incidence of male progeny, *him-8*(*e1489*) IV or *him-5*(*e1490*) V. Mutants recovered by EMS mutagenesis were outcrossed five times before use. Transgenic lines were generated by injection of plasmid DNA mixes into the hermaphrodite gonad. Integrated transgenic strains were generated with UV/trioxalen treatment (Kutscher and Shaham, 2014) (Sigma, T6137) and were outcrossed at least four times before imaging experiments. Most strains also had one of three integrated linker cell markers *qIs56*[*lag-2*p::GFP] V, *nsIs65*[*mig-24*p::Venus] X, or *nsIs650* [*mig-24*p::mKate2] X. Other alleles are as follows:

LGI

rab-2(*n3263*), *ced-1*(*e1735*), *cep-1*(*gk138*), *dpy-5*(*e907*)

LGII

cnt-1(*gk899634*), *cnt-1*(*tm2313*), *cdc-42*(*gk388*), *rab-7*(*ok511*)

LGIII

rab-35(*b1013*), *rab-35*(*tm2058*), *tbc-10*(*gk388086*), *unc-119*(*ed3*), *ttr-52*(*tm2003*), *ttr-52*(*tm2078*), *F23H11.4*(*gk585084*), *F23H11.4* (*gk165637*), *cnt-2*(*gm377*)

LGIV

arf-6(*tm1447*), *arf-6*(*ns388*), *arf-6*(*ns751*[D92N]), *arf-6*(*ns752*[D92N]), *arf-6*(*ns753*), *arf-6*(*ns760*[T44N]), *arf-6*(*ns761*[T44N]), *arf-6*(*ns762*[T44N]), *arf-6*(*ns763*[I42M;P43T]), *arf-6*(*ns765*[Q67L]), *arf-6*(*ns771*[Q67L]), *arf-6*(*ns753*), *arf-6*(*ns764*), *arf-6*(*ns767*), *arf-6*(*ns769*), *sand-1*(*or552*), *sand-1*(*ok1963*), *efa-6*(*ok3533*), *ced-10*(*n1993*), *ced-5*(*n1812*), *psr-1*(*ok714*), *psr-1*(*tm469*)

LGX

rme-4(*ns410*), *rme-4*(*ns412*), *rme-4*(*b1001*), *rme-4*(*tm1865*), *tbc-13*(*ok1812*), *piki-1*(*ok2346*), *him-4*(*e1267*), *git-1*(*ok1848*), *git-1*(*gk392605*), *gap-2*(*ok1001*)

Yeast

The yeast strain NMY51 (Dualsystems Biotech) was maintained at 30°C on YPAD plates for yeast two-hybrid assays. Yeast were plated on SD-Leu$^-$Trp$^-$ after transformation, and 5μl of OD_{600} = 0.4 of transformants were spotted on SD-Leu$^-$Trp$^-$ His$^-$ to test for interactions.

METHOD DETAILS

Forward Genetic Screen and Artificial Insemination

Young L4 hermaphrodites containing *qIs56* [*lag-2*p::GFP] and *him-5*(*e1490*) were mutagenized with 75 mM ethylmethanesulfonate (EMS, Sigma M0880) for 4h at 20°C. Animals were synchronized twice by bleaching, and male animals were enriched by passing through a 40 μm cell strainer (BD Falcon) passively for 20 min (Lewis and Fleming, 1995). Male animals fit more readily through the mesh than hermaphrodites and were enriched to ~88%. Animals were then scored under a fluorescent dissecting microscope (Leica) for presence of a linker cell by GFP. GFP-expressing animals were isolated away from hermaphrodites for 24h to accumulate spermatids within the gonad. Mutant males were immobilized on a dried agar pad under immersion oil, and spermatids removed with a needle containing SM buffer (50 mM HEPES, pH 7, 50 mM NaCl, 25 mM KCl, 5 mM $CaCl_2$, 1 mM $MgSO_4$, 1 mg/ml BSA) (LaMunyon and Ward, 1994). An N2 hermaphrodite with a single row of eggs was then immobilized on the same dried agar pad and gently injected with the collected sperm through the vulva. We typically tried to insert all spermatids into a single hermaphrodite. GFP$^+$ heterozygous progeny were collected, allowed to self fertilize, and linker cell persistence confirmed under a dissecting microscope.

Gene Identification

A combination of Hawaiian Snip-SNP mapping (Wicks et al., 2001) and whole genome sequencing (Zuryn et al., 2010) was using to identify *rme-4*(*ns410*), *rme-4*(*ns412*), and *arf-6*(*ns388*) using output from galign (Shaham, 2009). *rme-4* was confirmed by fosmid rescue using WRM0615bE09, and *arf-6* identification was confirmed by mutant cDNA expression and CRISPR alleles.

Linker Cell Survival and Corpse Persistence Assays

Linker cell death was scored as previously described (Blum et al., 2012). Briefly, unstarved gravid hermaphrodites were bleached to isolate embryos, which were allowed to hatch overnight in M9. Synchronized L1 animals were released on 9-cm NGM plates seeded with OP50 or HT115 *E. coli* containing the RNAi construct of interest on IPTG-RNAi plates. Male animals were isolated onto a new plate prior to the L4-to-adult transition based on full retraction of the male tail tip with rays visible under the unshed L4 cuticle. 24h later, these animals were mounted onto 2% agarose-water pads, anaesthetized in 25 mM sodium azide, and examined on an Axioplan 2 fluorescence microscope (Zeiss) with a 63x/1.4NA objective (Zeiss) and Nomarski optics. The linker cell was identified by location, morphology, and fluorescence from reporter transgenes. Cells were then scored as surviving, dead, or gone based on DIC morphology and fluorescence.

Generation of *arf-6* Alleles Using CRISPR-Cas9 Genome Editing

Alleles of *arf-6* were generated using the co-CRISPR-based genome editing method as previously described (Arribere et al., 2014). pDD162 was used as a vector backbone, and the following sgRNA sequences were added for each individual CRISPR attempt (D92N: 5' CTAAAAACCTGTCTCTATCAG 3'; T44N: 5' TCAGTGACCACAATGACGA 3'; Q67L 5' CTTCAGGACGTCGGCGGAC 3') to generate *arf-6* targeting vectors. A *dpy-10* sgRNA-pDD162-based vector was also generated (5' GCTACCATAGGCACCACGAG 3'). Single-stranded repair oligos were PAGE purified and ordered from Sigma (D92N: 5' aggaaaaaaaccaatttttccgcatttttcgcc taaaaacCTGTCTCTATtAGCaGCGTCCATCACAAAAATGAGCGCCTGAGTTCCTGTGTAATAATGTC 3'; T44N: 5' agCAATTCTGTA CAAACTGAAGCTCGGGCAATCAGTGACCACAATTCCGAacGTGGGCTTCAATGTGGAGACTGTCACGTATAAAAATATCAAATTCA ACGT 3'; Q67L 5' ggcctaaaaaccccccaaaaaccccaatttttcttcagGACGTCGGCGGACttGACAAAATTCGACCCCTCTGGCGACATTATTA CACAGGAACTCAGGCGCT 3', *dpy-10*(*cn64*): 5' CACTTGAACTTCAATACGGCAAGATGAGAATGACTGGAAACCGTACCGCATGC GGTGCCTATGGTAGCGGAGCTTCACATGGCTTCAGACCAACAGCCTAT 3' (Arribere et al., 2014). N2 animals were injected with the following mix: 50 ng/μl dpy-10 sgRNA, 50 ng/μl *arf-6* targeting vector, 20 ng/μl *dpy-10*(cn64) repair oligo, 20 ng/μl *arf-6* repair oligo in 1x injection buffer (20mM potassium phosphate, 3mM potassium citrate, 2% PEG, pH 7.5). F1 animals with Dpy or Rol phenotypes were picked to individual plates, indicating a CRISPR-based editing event had occurred. F1 animals were allowed to lay eggs, and then genotyped for successful co-conversion of the *arf-6* locus using PCR and restriction enzyme screening or Cel1 digestion of heteroduplex DNA (Ward, 2015). Non-Rol, non-Dpy F2 animals were then singled and homozygosed for the *arf-6* mutation.

Germline Transformation and Rescue Experiments

Plasmid mixes containing the plasmid of interest, co-injection markers, and pBluescript were injected into both gonads of young adult hermaphrodites (Mello and Fire, 1995). Injected animals were singled onto NGM plates and allowed to grow for two generations. Transformed animals based on co-injection markers were picked onto single plates, and screened for stable inheritance of the extra-chromosomal array. Only lines from different P0 injected hermaphrodites were considered independent. For cell-specific rescue experiments, animals expressing mCherry in either the linker cell or the U.l/rp cells were picked to a new plate at the early L4 stage, before linker cell death, to avoid bias. Isolated animals were then staged based on tail morphology under a white light microscope for appropriate linker cell scoring.

Plasmid Construction

Plasmids containing *lin-48*p, *mig-24*p, or transcriptional reporters were cloned using multi-piece one-step cloning into a modified pPD95.75 backbone lacking GFP. For CRISPR-related vectors, plasmids were generated using a site-directed plasmid mutagenesis protocol on pDD162 (Dickinson et al., 2013; Liu and Naismith, 2008). Yeast vectors were generated using traditional cloning from either a pLexA-N-terminus vector or a pGAL4AD-N-terminus vector (Dualsystems Biotech), and single amino acid change variants were generated using QuikChange (Agilent).

Protein Structures

The co-crystal structure of human Arf6 with the ArfGAP ASAP3 (PDB 3LVQ) was examined in Pymol (The PyMOL Molecular Graphics System, Version 1.2r3pre, Schrödinger, LLC.) in silico mutagenesis for D92N and I42M;P43T was performed and hydrophilic interactions tested within Pymol. Key residues noted in Figures 5A–5D in ASAP3 are conserved in *C. elegans* CNT-1, and those for Arf6 are conserved in *C. elegans* ARF-6.

Long-Term Imaging and Movie Generation

Early L4 male animals were imaged in a microfluidic device described in detail in (Keil et al., 2017). Animals were fed a constant flow of NA22 bacteria in S medium, supplemented with kanamycin (50 ng/μl) to prevent bacterial overgrowth. Animals were immobilized and imaged every 8 minutes for at least 20h. Mutant animals were typically imaged for > 30h. Exposure time and light intensity was held constant across strains when the same integrated transgene was imaged. Occasionally tail development was perturbed by the flow of medium and repeated immobilization procedures, and these animals were not included in subsequent analyses.

Deconvolution

Images were cropped to a region of interest surrounding the linker cell. We measured the point-spread function (PSF) of our optical setup using red (580/605nm) and green (505/515nm) fluorescent 200nm beads (ThermoFisher Scientific). Using these PSFs, we deconvolved the cropped fluorescence z-stacks using the classic maximum likelihood estimation (CMLE) algorithm with standard parameters (refractive index of imaging medium: 1.338) in the Huygens Essential software (Huygens Essential 3.7.1) by Scientific Volume Imaging (SVI).

Image Analysis

Image analysis was performed using custom-written MATLAB R2016b (Mathworks) scripts. To overlay imaging frames, we straightened each three-dimensional image stack using a previously published algorithm (Keil et al., 2017; Peng et al., 2008) based on a manually selected worm backbone in the DIC channel. To correct for small residual animal movements during multi-channel acquisition, obvious landmarks visible in the fluorescence channels, such as the cloaca, fluorescently labeled cells in the animal's tail, or vesicles within the U-cell descendants were then manually aligned to the DIC channel in each frame. Time-lapse movies were generated by centering all straightened, aligned images on the linker cell and cropping the entire movie to an appropriate size. Frames were removed from the movies whenever residual animal movement excessively blurred the images.

Fluorescence Intensity Quantification

All fluorescence intensity ratios (Figures 3, 5, 7, and S4) were quantified based on deconvolved and alignment-corrected z-stacks (see above). For each frame, we first selected the z-slice in which the linker cell or large linker cell fragment was maximally in focus in the DIC channel and used this slice for further quantification of fluorescence. In strains in which the linker cell was fluorescently labeled with the *mig-24* promoter, the linker cell outline was automatically detected using Otsu thresholding. Otherwise, the LC outline was manually selected based on its DIC features and its visible delineation in the respective fluorescence channels. Additionally, using the same fluorescence channel, we manually selected a cytoplasmic area in the U.l/rp cell in the same z-slice (at least 10pixels) for each frame. Average fluorescence values were then computed both, along the linker cell outline (membrane fluorescence value) and in the selected cytoplasmic region of the U.l/rp cell, allowing us to quantify enrichment of the fluorescently tagged proteins on the linker-cell-U.l/rp-cell interface compared to the cytoplasm of the U.l/rp cell.

RNAi Assay

pL4440 RNAi plasmids containing coding sequence to *rme-4* or *tbc-7* were isolated from the Ahringer Library (Kamath et al., 2003) (Source BioScience) and the coding sequence was confirmed by sequencing. These plasmids were grown at 37°C in HT115 bacteria,

which have a plasmid containing an inducible promoter driving T7 RNA polymerase. The bacteria were plated on NGM plates that had been supplemented with the antibiotic carbomycin and IPTG. One day later, synchronized L1 animals were plated on the RNAi plates and grown for two days before assaying for linker cell corpse persistence.

Yeast Two-Hybrid Assay

Strain and vectors used in assay were from the DUALHybrid Kit (Dualsystem Biotech). Bait cDNA was cloned into the pLexA plasmid and prey cDNA was cloned into pGAD vectors. These plasmids were cotransformed into NMY51 yeast strain using the lithium acetate method described in the DualHybrid manual. Selection was performed on SD plates lacking the amino acids leucine, tryptophan, and histidine.

Apoptotic Corpse Assay

We counted the number of apoptotic corpses in 3-fold embryos mounted on agar pads and examined at 63x using DIC (Nomarski optics). These corpses could be distinguished by their high refractility.

QUANTIFICATION AND STATISTICAL ANALYSIS

Statistical analysis was performed using GraphPad Prism. Statistical parameters including mean ± standard error of the proportion, mean ± SEM, and n are reported in the main text, figures and figure legends. Data is judged to be statistically significant when $p < 0.05$ by Fisher's exact test, χ^2-test, or student's t-test, where appropriate.

Genetic Data Analysis

When comparing a transgenic line to the parental strain, a minimum of three independent lines was scored. Approximately 100 animals from each of these lines were examined for linker cell defects, and compared to the parental strain using a Fisher's exact test to determine significance. For ease of presentation, we pooled the lines from a given experiment and displayed them on the relevant figure using mean ± SEM (N = 3, 4, or 5 lines). If only a subset of the three lines showed significance using a Fisher's exact test, we indicated this on the figure and figure legend.

DATA AND SOFTWARE AVAILABILITY

Custom image analysis and fluorescence intensity quantification scripts are available upon request.